Cell Reports

Resource

Morphological profiling of human T and NK lymphocytes by high-content cell imaging

Graphical abstract

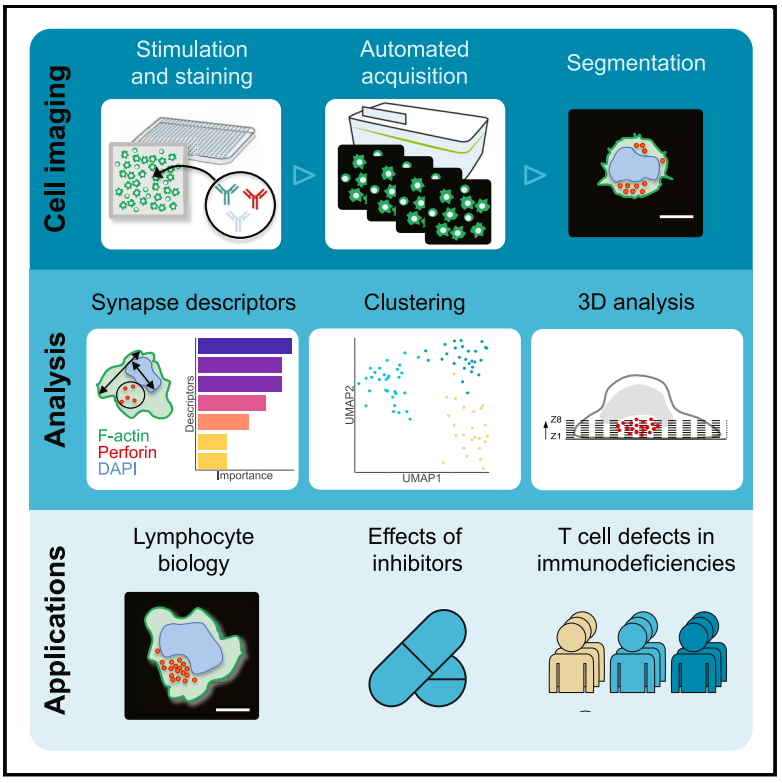

Authors

Yolla German, Loan Vulliard, Anton Kamnev, ..., Audrey Ferrand, Jörg Menche, Loïc Dupré

Correspondence

loic.dupre@inserm.fr

In brief

German et al. provide a workflow to study activation of cytotoxic T and NK lymphocytes by high-content confocal microscopy. Images are analyzed to characterize morphological variation in immunological synapses induced by actin compounds in primary cells as well as in CD8$^+$ T cells derived from ARPC1B- and WASP-deficient individuals.

Highlights

- Cytotoxic lymphocytes can be profiled in depth using high-content imaging
- Morphological changes are identified with dedicated analytical tools
- Distinct immunological synapse alterations in ARPC1B- and WASP-deficient T cells
- 3D distribution of lytic granules is impaired in ARPC1B-deficient CD8$^+$ T cells

German et al., 2021, Cell Reports *36*, 109318
July 6, 2021
https://doi.org/10.1016/j.celrep.2021.109318

CellPress

Cell Reports

CellPress
OPEN ACCESS

Resource

Morphological profiling of human T and NK lymphocytes by high-content cell imaging

Yolla German,[1,2,11] Loan Vulliard,[3,4,11] Anton Kamnev,[2,5] Laurène Pfajfer,[1,2] Jakob Huemer,[2,6] Anna-Katharina Mautner,[2,5] Aude Rubio,[7] Artem Kalinichenko,[2,6] Kaan Boztug,[2,3,6,8,9] Audrey Ferrand,[7] Jörg Menche,[3,4,10] and Loïc Dupré[1,2,5,12,*]

[1]Toulouse Institute for Infectious and Inflammatory Diseases (INFINITy), INSERM UMR1291, CNRS UMR5051, Toulouse III Paul Sabatier University, Toulouse, France
[2]Ludwig Boltzmann Institute for Rare and Undiagnosed Diseases (LBI-RUD), Vienna, Austria
[3]CeMM Research Center for Molecular Medicine of the Austrian Academy of Sciences, Vienna, Austria
[4]Department of Structural and Computational Biology, Max Perutz Labs, University of Vienna, Vienna, Austria
[5]Department of Dermatology, Medical University of Vienna, Vienna, Austria
[6]St. Anna Children's Cancer Research Institute (CCRI), Vienna, Austria
[7]IRSD, Université de Toulouse, INSERM, INRA, ENVT, UPS, 31024 Toulouse, France
[8]Department of Pediatrics and Adolescent Medicine, Medical University of Vienna, Vienna, Austria
[9]St. Anna Children's Hospital, Department of Pediatrics and Adolescent Medicine, Medical University of Vienna, Vienna, Austria
[10]Faculty of Mathematics, University of Vienna, Vienna, Austria
[11]These authors contributed equally
[12]Lead contact
*Correspondence: loic.dupre@inserm.fr
https://doi.org/10.1016/j.celrep.2021.109318

SUMMARY

The immunological synapse is a complex structure that decodes stimulatory signals into adapted lymphocyte responses. It is a unique window to monitor lymphocyte activity because of development of systematic quantitative approaches. Here we demonstrate the applicability of high-content imaging to human T and natural killer (NK) cells and develop a pipeline for unbiased analysis of high-definition morphological profiles. Our approach reveals how distinct facets of actin cytoskeleton remodeling shape immunological synapse architecture and affect lytic granule positioning. Morphological profiling of $CD8^+$ T cells from immunodeficient individuals allows discrimination of the roles of the ARP2/3 subunit ARPC1B and the ARP2/3 activator Wiskott-Aldrich syndrome protein (WASP) in immunological synapse assembly. Single-cell analysis further identifies uncoupling of lytic granules and F-actin radial distribution in ARPC1B-deficient lymphocytes. Our study provides a foundation for development of morphological profiling as a scalable approach to monitor primary lymphocyte responsiveness and to identify complex aspects of lymphocyte micro-architecture.

INTRODUCTION

Recent advances in high-content imaging (HCI) allow morphological profiling of cell populations at a rich level of detail, providing an integrative readout for complex biological events. HCI is particularly suitable for systematic analysis of cellular phenotypes. It is employed widely in cancer and toxicology research on adherent cell lines to evaluate cellular fitness and viability upon drug treatment or genetic alterations (de Groot et al., 2018; Joshi and Lee, 2015; Papakonstantinou and O'Brien, 2014; Priestley et al., 2019; Wu and Li, 2018). HCI is also a powerful approach for identification of novel systemic properties of cells (Bryce et al., 2019; Caldera et al., 2019; Heigwer et al., 2018; Mattiazzi Usaj et al., 2020). To the best of our knowledge, HCI has not yet been applied to study immune cell populations, which are traditionally studied by flow cytometry. Because these highly specialized cells adopt distinctive morphologies and structures to sustain their various immuno-surveillance tasks, HCI would be highly relevant to monitor immune cell shape remodeling upon activation. In particular, the immunological synapse (IS) is a complex structure that sets lymphocyte activation and function during encounters with antigen-presenting cells and target cells. Low-throughput microscopy approaches have revealed that the IS is characterized by a symmetrical architecture consisting of concentric rings of F-actin and integrins, whereas the antigen receptors occupy a central position (Grakoui et al., 1999; Monks et al., 1998). The lymphocyte spreading associated with IS assembly and organization relies on dynamic rearrangements of the actin cytoskeleton (Dustin and Long, 2010). In cytotoxic lymphocytes, including $CD8^+$ T cells and natural killer (NK) cells, the IS is particularly important because it sustains polarized delivery of cytolytic molecules, such as perforin and granzymes, toward target cells (Somersalo et al., 2004). The study of IS organization has remained low throughput and has been restricted to analysis of a limited number of morphological measurements. A more systematic and in-depth assessment of the IS would leverage this structure as a pivotal readout for characterization of lymphocyte activation.

In this study, we report implementation of a scalable HCI approach combining confocal imaging of human T and NK cells stimulated over 2D surfaces functionalized with ICAM-1 and stimulatory antibodies (Abs), and high-dimensional profiling and clustering of IS morphologies. Comparison of lymphocytes treated with drugs affecting different facets of actin cytoskeleton remodeling highlights a variety of morphological alterations and effects on lytic granule distribution and degranulation. Application of our HCI pipeline to lymphocytes isolated from human blood reveals distinct morphological profiles in individual healthy donors. Furthermore, our method allows discrimination of synapse defects in untransformed $CD8^+$ T cells from individuals with related deficiencies in the actin regulators ARPC1B and WASP, illustrating its potential to identify disease-specific morphological signatures. Single-cell analysis points to a loss of relationship between actin radial distribution and lytic granule dispersion as a possible explanation for the reduced cytotoxic activity of ARPC1B-deficient $CD8^+$ T cells. This inspired complementary time-lapse recording of actin and lytic granule dynamics, indicating unstable positioning of the lytic granule pool in ARPC1B-deficient $CD8^+$ T cells. Finally, we detail our experimental and computational methods and provide a reproducible analysis environment to enable their application to other study models.

RESULTS

Morphological profiles of T and NK cell ISs

To systematically analyze the morphological profile of T and NK cells, we designed a custom HCI workflow consisting of seeding cells on stimulatory surfaces in microwells of 96- or 384-well plates with subsequent fixation and staining for nuclei, the actin cytoskeleton, and perforin or LFA-1 with combinations of fluorescent dyes and Abs. Confocal images were acquired on an Opera Phenix high-content screening system equipped with a water immersion 40× objective and 4 scientific complementary metal-oxide-semiconductor (sCMOS) cameras. Images were acquired along 8 Z-planes with a 0.5-μm interval starting from the cell-substrate interface and were analyzed with CellProfiler (McQuin et al., 2018) to automatically segment individual cells and extract quantitative morphological descriptors based on the different fluorescent markers (Figure 1A). As proof of concept, we applied our approach to NK-92 and Jurkat cells, two human cell lines commonly used as models for NK cells and T cells, respectively. Cell morphologies were compared upon interaction with a poly-L-lysine (PLL)-coated or stimulatory surface with the LFA-1 ligand ICAM-1 and stimulatory Ab evoking IS assembly. Upon co-stimulation with ICAM-1 and anti-NKp30/NKp46 Ab, NK-92 cells spread, emitted F-actin-rich peripheral pseudopodia, and gathered perforin-containing granules toward the center of the cell-substrate interface, as indicated by their detection in proximity of the cell-substrate interface (Figure 1B; Figure S1A). These observations are in line with the hallmarks of the IS in cytotoxic lymphocytes (Dieckmann et al., 2016; Dustin and Long, 2010), validating our high-throughput stimulation and staining procedure. We first assembled a curated set of descriptors to serve as the basis for morphological profiling. Based on literature describing the IS and reporting polarization of F-actin and lytic granules in NK cells (Krzewski and Coligan, 2012; Mace et al., 2012, 2014), we integrated morphological descriptors for F-actin and perforin staining and completed them with nuclear measurements via DAPI staining (Figure 1C; Table S1). The selected descriptors were extracted as mean values per field of view averaged across 3 experiments. The increases in F-actin intensity and cell area were prominent features of the stimulation compared with the PLL condition. Furthermore, the number of perforin-containing granules detected at the cell-substrate interface increased upon stimulation, which is indicative of their enrichment toward the IS. We detected relative spreading of the area covered by lytic granules, supporting the notion of multiple docking domains at the synapse (Brown et al., 2011). Notably, our analysis also highlights an increase in nucleus area as a typical feature of the IS in stimulated NK-92 cells. The nucleus area increased noticeably along with F-actin intensity when assessed across three experiments (Figure 1D), suggesting that cortical actin is associated with mechanical tensions that may flatten the nucleus. Of note, the absolute values for F-actin intensity were higher in one of the 3 experiments, possibly resulting from differences in staining quality. This indicates that absolute values for staining intensities across experiments should be considered with caution. Consequently, all further comparisons of samples and treatments were done within the same staining/acquisition batches and within the same plates. To ensure that no morphological heterogeneity across cells was overlooked by comparing mean values per field of view, F-actin intensity was assessed on a per-cell basis (Figure 1E). The unimodal increase in F-actin intensity driven by stimulation of NK-92 cells indicates a relatively homogeneous IS assembly, which validates our approach.

In parallel, the HCI workflow was applied to Jurkat cells, which were stimulated with ICAM-1 and anti-CD3 Abs. We selected, in this instance, 12 measurements to constitute our curated set of morphological descriptors, which pertained to F-actin, LFA-1, and DAPI staining to monitor hallmarks of the T cell IS (Dustin and Long, 2010). Because Jurkat cells do not express perforin, the LFA-1 integrin was stained instead. Compared with the neutral PLL surface, ICAM-1/anti-CD3 Ab stimulation led to cell spreading, assembly of a peripheral F-actin ring-like structure, and distribution of the integrin LFA-1 as a dense array of clusters at the cell-substrate interface (Figure 1F; Figure S1B), which are characteristic for the IS (Dustin and Long, 2010; Houmadi et al., 2018). Our quantification over multiple fields showed that, similar to NK-92 cells, F-actin intensity and cell area are prominent features of the Jurkat cell IS (Figure 1G; Table S2). Moreover, LFA-1 intensity and LFA-1 area also increased upon stimulation, and we noted that F-actin and LFA-1 intensities correlated in individual fields of view with a Pearson correlation coefficient of 0.50 (Figure 1H). At the single-cell level, F-actin clearly increased in response to ICAM-1 and anti-CD3 Ab stimulation despite noticeable heterogeneity (Figure 1I). The data collected on assembly of the IS in NK-92 and Jurkat cells reveal commonalities, such as a raise in F-actin intensity and cell spreading, whereas Jurkat cells, but not NK-92 cells, became rounder upon co-stimulation of LFA-1 and T cell receptors (TCR). Furthermore, although NK-92 cells flattened their nuclei, this effect was not observed in Jurkat cells, indicating a distinct cell spreading behavior in each cell line. Such differences among the 2 cellular models might be due to distinct IS architectures or

CellPress
OPEN ACCESS

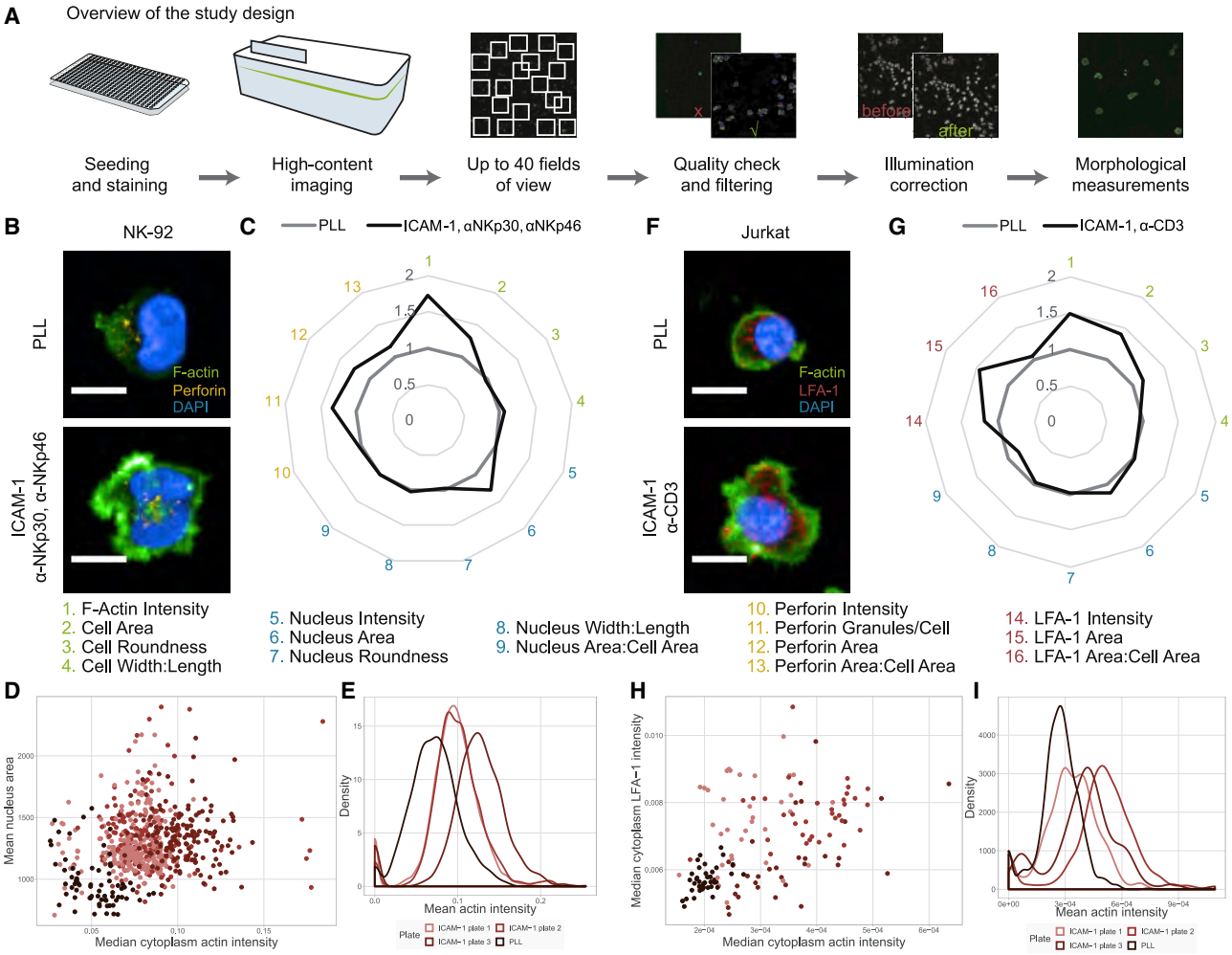

Figure 1. HCI of the IS in lymphocytic cell lines

(A) Schematic of the HCI pipeline.

(B) Representative images of NK-92 cells seeded on poly-L-lysine (PLL) or ICAM-1 plus anti-NKp30/NKp46 Abs, stained for F-actin (green), perforin (yellow), and the nucleus (DAPI). Scale bars, 10 μm.

(C) Selected IS features analyzed as fold change of ICAM-1 plus anti-NKp30/NKp46 Abs over PLL. The data represent the mean of three separate experiments (n = 933–5,860 cells).

(D) Mean nucleus area in pixels and median F-actin intensity per image across PLL and ICAM-1 plus anti-NKp30/NKp46 Ab conditions.

(E) F-actin intensity distribution per cell across PLL and ICAM-1 plus anti-NKp30/NKp46 Ab conditions.

(F) Representative images of Jurkat cells on PLL or ICAM-1 plus anti-CD3 Abs, stained for F-actin (green), LFA-1 (red), and the nucleus (DAPI). Scale bars, 10 μm.

(G) Selected IS features analyzed as fold change of ICAM-1 plus anti-CD3 Abs over PLL. The data represent the mean of triplicates (n = 125–940 cells).

(H) Median F-actin and LFA-1 intensity per image across PLL and ICAM-1 plus anti-CD3 Ab conditions.

(I) F-actin intensity distribution per cell across PLL and ICAM-1 plus anti-CD3 Ab conditions.

See also Figure S1 and Tables S1 and S2.

different kinetics of the IS assembly, as highlighted recently by a comparison of primary T and NK cells (Carisey et al., 2018). Overall, our data validate the reliability and power of our HCI pipeline for automated morphological profiling of stimulated lymphocytes with high spatial resolution.

Cytoskeleton drugs induce distinct alterations of the NK cell IS

In line with the role of actin remodeling in sustaining IS assembly (Dustin and Cooper, 2000), our data point to the rise in F-actin content as a prominent feature of this process. To gain a systematic view of how distinct facets of actin dynamics, including polymerization, coupling to myosin, and branching or elongation of filaments, might contribute to assembly of ISs in cytotoxic lymphocytes, we performed morphological profiling of NK-92 cells stimulated with ICAM-1 and anti-NKp30/NKp46 Abs upon treatment with three concentrations of the drugs latrunculin B, jasplakinolide, blebbistatin, Y-27632, CK-869, wiskostatin, and SMIFH2. To compare morphological alterations, we used curated morphological descriptors identified previously (Figures 2A and

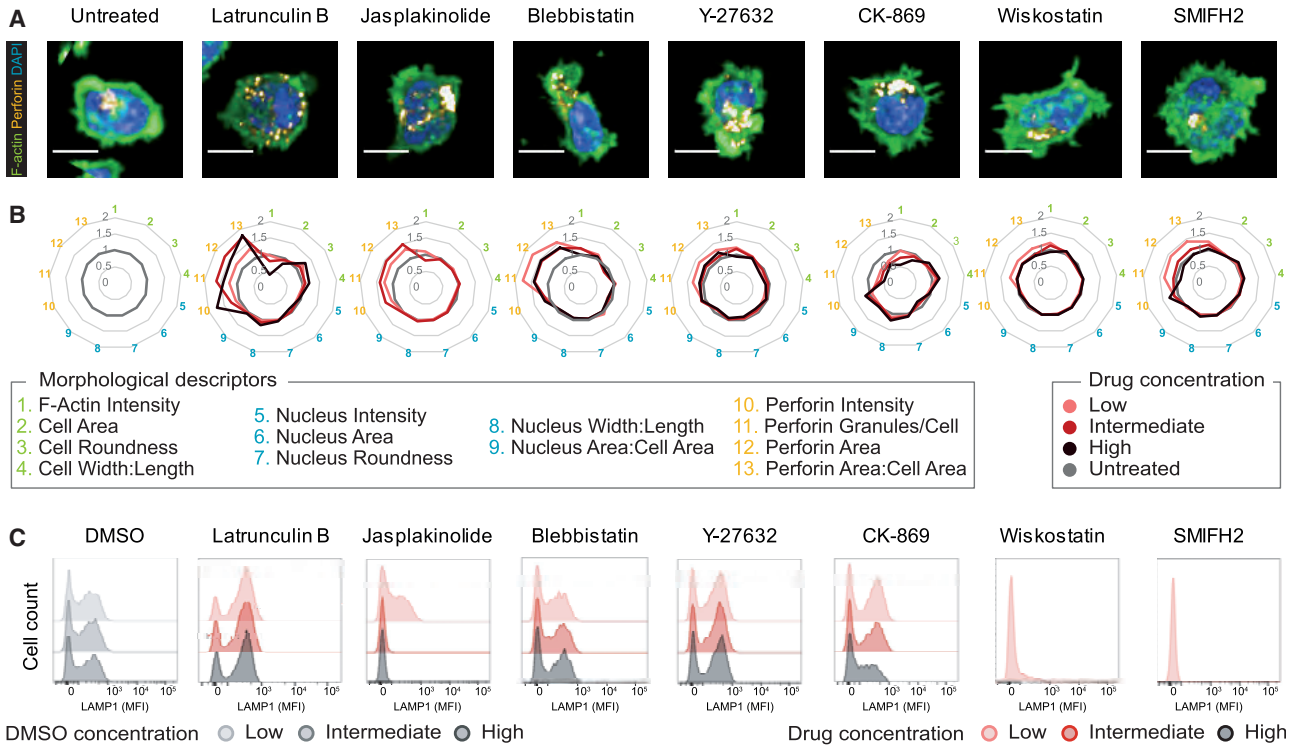

Figure 2. Comparative analysis of the effect of actin-targeting drugs on lytic granule distribution and exocytosis in NK-92 cells

(A and B) Representative images (A) and graphs (B) representing the fold change of IS descriptors for NK-92 cells seeded on ICAM-1, anti-NKp30, and anti-NKp46, stained for F-actin (green), perforin granules (yellow), and nuclei (blue) and treated with three concentrations of latrunculin B, jasplakinolide, blebbistatin, Y-27632, CK-869, wiskostatin, and SMIFH2 with respect to the untreated control. The data represent the mean of triplicates for each concentration (1,425–5,541 cells). Scale bars, 10 μm.

(C) Evaluation of LAMP-1 expression on NK-92 cells upon stimulation and treatment with the indicated drugs.

2B). This analysis was complemented with measurement of LAMP-1 surface exposure to assess the effects of the tested drugs on lytic granule exocytosis (Figure 2C; Figure S2). As expected, inhibition of actin polymerization by latrunculin B led to a concentration-dependent decrease in F-actin intensity (Figures 2A and 2B), validating our approach. Although cell spreading was not fully impeded, as revealed by only a minor reduction in cell area, cell roundness increased, possibly because of a reduction in peripheral actin-rich protrusions. Latrunculin B treatment elicited an increase in the number and area of perforin granules. In parallel, the treated cells exhibited increased LAMP-1 surface exposure upon stimulation (Figure 2C). This suggests that the loss of F-actin density evoked by latrunculin B treatment impaired the filter function of the F-actin cortical network (Carisey et al., 2018; Mace et al., 2012), resulting in uncontrolled and poorly polarized lytic granule exocytosis. F-actin stabilization by jasplakinolide did not result in an increase in F-actin intensity (Figures 2A and 2B). Treatment with an intermediate concentration of 1 μM led to a mild decrease in F-actin intensity, possibly through competition of the drug with phalloidin-AF488 for F-actin binding (Bubb et al., 1994). Different from latrunculin B, jasplakinolide appeared to not alter the cell morphological descriptors, implying that F-actin polymerization, but not stabilization, is crucial for NK cell IS assembly. A higher concentration of 2.5 μM jasplakinolide was tested but discarded because of its apparent detrimental effect on cell viability. Treatment with jasplakinolide elicited an increase in the perforin-related descriptors, corresponding to more, larger, and brighter granules. In contrast to latrunculin B, jasplakinolide treatment was associated with severe impairment of lytic granule exocytosis (Figure 2C), indicating accumulation of lytic granules at the synapse plane. This confirms that actin turnover is required for lytic granule exocytosis (Carisey et al., 2018; Lyubchenko et al., 2003). Inhibition of acto-myosin contractility via the Rho-associated protein kinase (ROCK)-myosin pathway using blebbistatin or Y-27632 yielded overlapping effects with a mild increase in F-actin intensity and mild decrease in cell roundness (Figures 2A and 2B), suggesting minor control over overall assembly of the IS. Treatment with blebbistatin and Y-27632 increased the number of granules detected at the synapse and the area they occupied but had no effect on LAMP-1 surface exposure (Figure 2C; Figure S2). In partial contrast with previous reports regarding the role of myosin IIA in promoting lytic granule fusion with the cell membrane (Andzelm et al., 2007; Sanborn et al., 2009), our data suggest that acto-myosin contractility contributes to lytic granule positioning at the IS without affecting degranulation per se. Given the prominent role of actin polymerization in controlling the IS, we compared the relative contribution of actin branching and actin filament elongation, employing inhibitors of the ARP2/3 complex (CK-869), WASP (wiskostatin), and formins (SMIFH2). CK-869 treatment led to a concentration-dependent

decrease in F-actin intensity and cell shape alterations, whereas wiskostatin and SMIFH2 treatments resulted in a modest increase in F-actin intensity without distinct alteration of cell shape descriptors (Figures 2A and 2B). A specific property of CK-869 treatment was a reduction in the number of and area covered by perforin granules, possibly reflecting the inability of CK-869-treated cells to polarize lytic granules toward the stimulatory surface because of defective IS assembly. In agreement, this was accompanied by a dose-dependent reduction in lytic granule exocytosis (Figure 2C; Figure S2), as reported previously (Randzavola et al., 2019). Low-concentration wiskostatin and SMIFH2 treatments resulted in an increase in perforin intensity and area, supporting a role of WASP and formins in lytic granule positioning at the IS (Houmadi et al., 2018; Butler and Cooper, 2009). The effect of these treatments on degranulation was not conclusive because cell toxicity was observed over the 4 h of the LAMP-1 surface exposure experiments. Overall, our comparative analysis shows that lytic granule distribution at the NK IS is dependent on the integrity of various facets of actin dynamics, supporting the notion that multiple actin-dependent steps control lytic granule docking and exocytosis (Mace et al., 2014). We further identify the ARP2/3 complex as playing a dominant role in driving actin polymerization, sustaining IS assembly, and controlling lytic granule positioning.

High-definition morphological profiling of NK cells upon drug treatment

To further enrich the morphological analysis of the IS in the context of drug treatment, the initial set of curated descriptors was expanded to include all available measurements. These included various descriptors of cell shape, staining intensity distributions and textures, as well as descriptors of heterogeneity, such as standard deviation of the aforementioned measurements per field of view, because they were found to be informative in other morphological profiling studies (Breinig et al., 2015; Bryce et al., 2019; Caldera et al., 2019; Rohban et al., 2019). From 1,898 initial measurements, a set of 383 morphological descriptors was retained following filtering of non-informative and redundant descriptors. By opposition to the curated morphological descriptors used previously, we further refer to this new set as comprehensive morphological descriptors. To visualize and quantify the significance of morphological changes upon drug treatment compared with untreated cells, we applied a uniform manifold approximation and projection (UMAP) dimensionality reduction to these morphological profiles. This allows visualization of the relation between the morphology displayed on each field of view in a 2D morphological space, summarizing the variation on all the 383 comprehensive morphological descriptors (Figure S3A). We sorted these measurements based on the cellular compartment (nucleus, cytoplasm, or granules) and the concept they described, such as granularity or shape. By examining the relation between them, we observed no strong clustering, suggesting that the different types of measurements acquired and the different compartments studied provided complementary and non-redundant information about the IS changes occurring across treatments (Figure S3B). This also implied that none of these morphological descriptors were repeating technical confounders, such as experimental plate position effect or cell density, because the confounders were more similar to each other than to any other descriptor. The morphological space revealed that latrunculin B, jasplakinolide, and CK-869 treatments were clustered away from the untreated cells and from one another, most likely because of these drugs having prominent and distinct effects on the ability of NK-92 cells to assemble the IS (Figures 3A, 3B, and 3E). In comparison, morphologies of cells treated with blebbistatin, Y-27632, wiskostatin, and SMIFH2 appeared to be less distinct from the untreated condition and to cluster in close vicinity of one another (Figures 3C, 3D, 3F, and 3G). The three concentrations assayed per treatment fell into distinct sub-clusters, clearly indicating dose-dependent effects, as detailed for CK-869 and SMIFH2 (Figures S3C and S3D). All drug-evoked morphological profiles were found to be significantly distant from the untreated state. Indeed, the median robust Mahalanobis distances between the fields of view of treated cells and their matching negative controls are larger than expected at random (Figure S3E; Hutz et al., 2013; Rousseeuw and Leroy, 1987). To get insight into the nature of the morphological changes identified in this experiment and pinpoint which of these changes are hallmarks of the chemical treatments, we trained a random forest classifier (Breiman, 2001). This tells us (1) whether the changes are strong enough to result in good model performance and (2) which features are essential to delimit each class. The image set was split to carry out parameter optimization and validate the performance of the model by cross-validation. The classifier achieved good performance, as shown on the confusion matrix (Figure 3H), with an F_1 score and an accuracy of 0.89 and 89%, respectively, which highlights the relevance of the comprehensive morphological descriptors to characterize treatment effects. Most drugs were predicted with high accuracy based on the corresponding image measurements, whereas the morphological effects of blebbistatin and Y-27632 were more challenging to distinguish, in line with their highly related mechanism of action. The importance of each descriptor for classification was proxied by the average increase in accuracy obtained by including the given variable in a decision tree. In particular, our analysis shows that CK-869 treatment mostly affected nucleus and cytoplasm shape descriptors (Figure 3I), whereas SMIFH2 treatment altered radial intensity distributions in the cytoplasm (Figure 3J). Only four measurements described intensities in the cytoplasm within the comprehensive descriptors. Interestingly, those few descriptors, on average, increased model accuracy the most, strengthening the necessity, but not sufficiency, of actin intensity measurements to profile the IS. Descriptors pertaining to lytic granules also played a determinant role in reinforcing model accuracy, providing further evidence of a tight regulation of lytic granule distribution at the IS. In comparison, we trained a classifier only on the curated descriptors used previously (Figure S3f). The overall accuracy of 69% and F_1 score of 0.70 confirmed that these descriptors characterize relatively well the morphological effects of the actin drugs, but the unbiased comprehensive approach offers a considerably higher definition of the morphological description of the IS. It also confirmed F-actin intensity as a major discriminating feature and identified cell eccentricity and roundness as key features to account for the morphological alterations induced by the drugs (Figure S3G). Our data therefore demonstrate the ability of the unbiased profiling to identify relevant

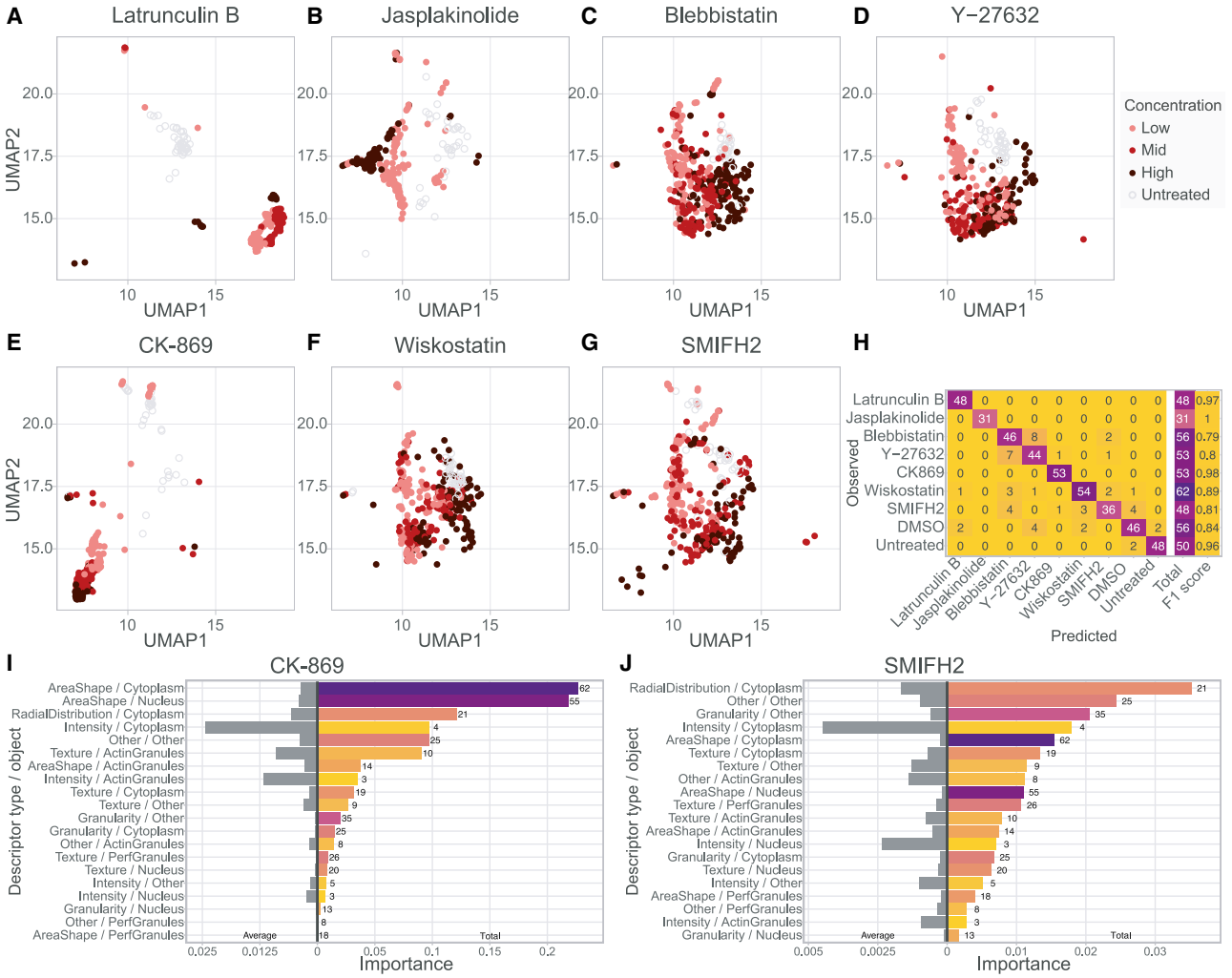

Figure 3. Morphological profiling of the NK cell IS upon drug treatment

(A–G) NK-92 cells were treated with the indicated drugs. Corresponding images were analyzed with CellProfiler for an array of measurements and visualized using UMAP to position drug-treated cells with respect to untreated cells from the same row.

(H) Confusion matrix and class-wise performance on held-out data of a random forest model trained to predict drug treatment based on the morphology of NK-92 cells seeded on ICAM-1, anti-NKp30, and anti-NKp46.

(I and J) Total and average importance for prediction of morphological features per measurement type and biological object described of NK-92 cells seeded on ICAM-1, anti-NKp30, and anti-NKp46 and treated with (I) CK-869 or (J) SMIFH2.

In (H)–(J), a darker color indicates a higher number of images or descriptors for a given box, and the corresponding count is provided alongside.

spatially localized events and characterize perturbed cell states with high-definition power.

Morphological profiling of primary human NK cells upon drug treatment

We next explored the applicability of HCI to study primary human lymphocytes. For that purpose, NK cells were purified from the peripheral blood of three normal donors, treated with four concentrations of CK-869 or SMIFH2, and stimulated with ICAM-1 and anti-NKp30/NKp46 Abs (Figure 4A). We disregarded PLL as a control surface because primary NK cells appeared to strongly remodel their morphology over this surface, in line with recent observations (Santos et al., 2018). The stimulatory surface promoted an actin-rich IS with lytic granules concentrated in one area on the side of the nucleus. The four concentrations of CK-869 caused a marked decrease in F-actin intensity in the NK cells from the three donors, demonstrating the capacity of morphological profiling to detect actin cytoskeleton alterations in primary lymphocytes. Notably, the area covered by the perforin granules, taken as an absolute value or divided by the cell area, was increased in the CK-869-treated NK cells from the three donors, showing a clear dose-dependent response (Figure 4B). This effect is opposite to what was measured in NK-92 cells, highlighting contrasting responses of model cell lines and primary cells. Moreover, the four concentrations of SMIFH2 also caused a decrease in F-actin intensity in the

CellPress
OPEN ACCESS

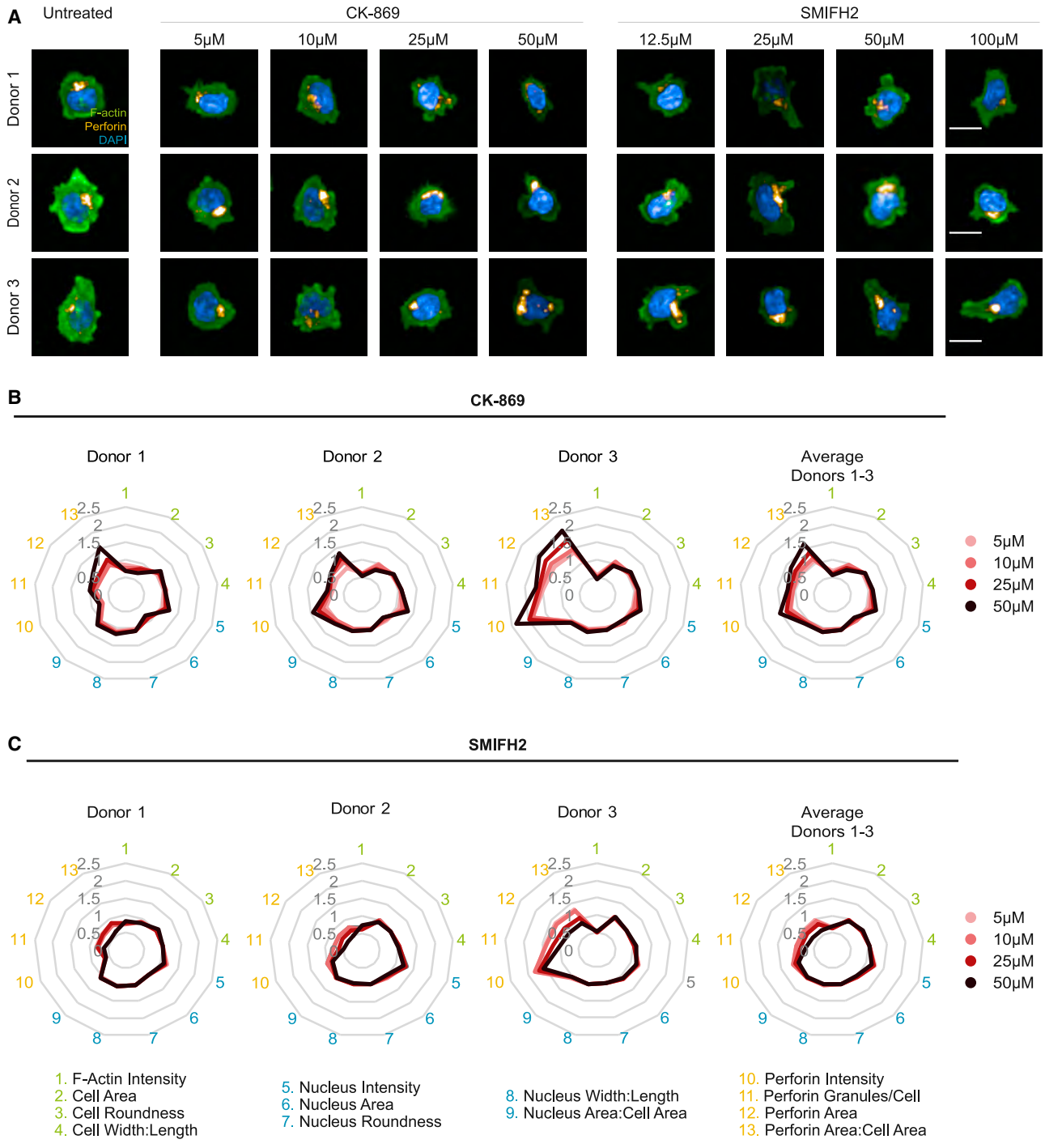

Figure 4. CK-869 and SMIFH2 treatments alter IS architecture and lytic granule polarization in primary NK cells

(A) Representative images of primary NK cells isolated from peripheral blood mononuclear cells (PBMCs) of three normal donors seeded on ICAM-1, anti-NKp30, and anti-NKp46, stained for F-actin (green), perforin granules (yellow), and nuclei (blue) and left untreated or treated with four concentrations of CK-869 or SMIFH2. Scale bars, 10 μm.

(B and C) Graphs representing the fold changes of IS parameters of primary NK cells treated with (B) CK-869 and (C) SMIFH2 with respect to untreated controls. The data represent the mean of 4 replicates for each drug concentration (60–409 cells).

NK cells from the three donors, highlighting the importance of formins for actin remodeling at the IS of primary NK cells (Figure 4C). SMIFH2 treatment also strongly affected the distribution of perforin granules. Remarkably, dose-dependent reductions in perforin granule number and covered area were observed in NK cells from the first two donors and to a lesser extent in the NK cells from the third donor. Therefore, although inhibition of actin branching and actin elongation yields comparable net decreases in polymerized actin, these treatments differentially affect the distribution of lytic granules. Those observations highlight the potential of HCI to identify complex relationships between cytoskeleton remodeling and organelle trafficking. In addition, HCI reveals features underlying inter-donor variability upon stimulation and treatment of lymphocyte populations.

Distinct IS defects in CD8$^+$ T cells from ARPC1B- and WASP-deficient individuals

To broaden the scope of application of HCI and assess its relevance in hematological disease settings, we implemented morphological profiling of CD8$^+$ T cells isolated from individuals suffering from two related inborn errors of immunity (IEIs) caused by mutations in *ARPC1B* and *WAS*, which encode a subunit of the ARP2/3 complex and the ARP2/3 activator WASP, respectively. Cells from three ARPC1B-deficient and three WASP-deficient individuals and three normal donors were stimulated with ICAM-1 anti-CD3 Abs and stained for F-actin, perforin, the nucleus, and CD8 (for exclusion of contaminating non-CD8$^+$ T cells). Analysis of 13 curated morphological descriptors highlighted that F-actin intensity was decreased in cells from ARPC1B- and WASP-deficient individuals compared with cells from normal donors (Figures 5A and 5B). This decrease was observed in all individuals (Figures S4A–S4D). When examining the mean values of the descriptors pertaining to shape and the nucleus, T cells from ARPC1B-deficient and WASP-deficient individuals did not appear to display striking alterations (Figure 5B; Figures S4A–S4D). Remarkably, the number of detected perforin granules and, consequently, the average fraction of the cell area they occupied was increased in T cells from ARPC1B- and WASP-deficient individuals (Figure 5B). This was the case for all three WASP-deficient individuals and two of three ARPC1B-deficient individuals (Figures S4A–S4D). The effect of these natural deficiencies on lytic granule positioning is reminiscent of the increase in perforin descriptors observed above upon treatment of primary NK cells with the ARP2/3 inhibitor CK-869. Our findings also align with a previous characterization of IS defects in WASP-deficient (Houmadi et al., 2018) and ARPC1B-deficient individuals (Brigida et al., 2018; Randzavola et al., 2019). We took advantage of the side-by-side HCI analysis of T cells from the 2 disease entities to identify specific traits. We selected a comprehensive set of 306 informative descriptors we projected onto a morphological space with UMAP. This analysis evidenced a marked segregation of affected individuals from control donors but also among the 2 disease entities (Figure 5C). This indicates that, beyond reduced F-actin intensity and altered distribution of lytic granules, additional morphological descriptors might be differentially altered in ARPC1B- and WASP-deficient CD8$^+$ T cells. Applying a random forest model, we then tested the ability of our approach to distinguish cells from normal donors and from each of the two deficiencies. Near-perfect classification was obtained on the validation set of images, with an overall accuracy of 96% and F_1 score of 0.96 (Figure 5D), confirming that the ARPC1B and WASP deficiencies were associated with distinct morphological alterations. The categories of descriptors selected most often by the random forest model indicated that ARPC1B-deficient T cells were mostly recognized on the basis of descriptors pertaining to the cell periphery (referred to as ''cytoplasm'' and corresponding to the cell mask extending beyond the nucleus projection) (Figures 5E and 5F). These descriptors included mean and standard deviation of radial distribution of actin intensities as well as shape- and texture-related parameters. These descriptor classes also accounted partly for the discrimination of WASP-deficient T cells. However, these cells were mostly recognized on the basis of descriptors pertaining to the cell center (referred as to ''nucleus'' and corresponding to the nucleus projection mask). These descriptors included shape- and texture-related parameters. This ranking of discriminative descriptor classes reveals distinct morphological signatures in T cells with the related ARPC1B and WASP deficiencies that suggest non-overlapping spatial distribution of associated defects in the context of IS assembly.

Altered lytic granule distribution in ARPC1B-deficient CD8$^+$ T cells revealed by single-cell analysis

CD8$^+$ T cells isolated from an ARPC1B-deficient individual have been shown recently to be unable to kill target cells, and this impairment was associated with a combination of defects in lamellipodium formation, centrosome polarization, lytic granule dispersion, and expression of TCR, CD8, GLUT1, and granzyme B (Randzavola et al., 2019). Here we sought to exploit the confocal resolution and single-cell granularity of our HCI approach to investigate in more detail how defective actin remodeling may relate to aberrant distribution of lytic granules in the context of ARPC1B deficiency. We confirmed that ARPC1B-deficient CD8$^+$ T cells have reduced cytotoxic activity (Figure S5D) with evidence of aberrant morphology upon contact with target cells (Figure S5E). However, the CD8$^+$ T cells from the ARPC1B-deficient individuals considered in our study expressed normal levels of the TCR, CD8, perforin, and granzyme B (Figure S5C), indicating that the killing defect was not related to aberrant expression of these molecules. We first took advantage of the confocal resolution of our imaging approach to quantify lytic granule distance from the synaptic plane. Eight confocal slices spanning 3.5 μm above the cell-substrate interface were acquired in cells stained for perforin, F-actin, and the nucleus. Our analysis indicates that lytic granules are detected all along the considered Z-planes with enrichment in z layers 3 to 5 corresponding to the layer 1–2 μm from the synapse plane (Figure 6A). Clearly, polarization of the lytic granules toward the synapse plane was not altered in CD8$^+$ T cells from the 2 ARPC1B-deficient individuals, implying that ARPC1B deficiency in the 2 studied individuals did not prevent lytic granule positioning toward the IS. Next we exploited the power of our HCI approach in collecting morphological descriptors pertaining to individual cells to extract relations between actin and perforin features at a single-cell level. Using multiple linear regression, we estimated the relationship between key actin-based descriptors and lytic granule

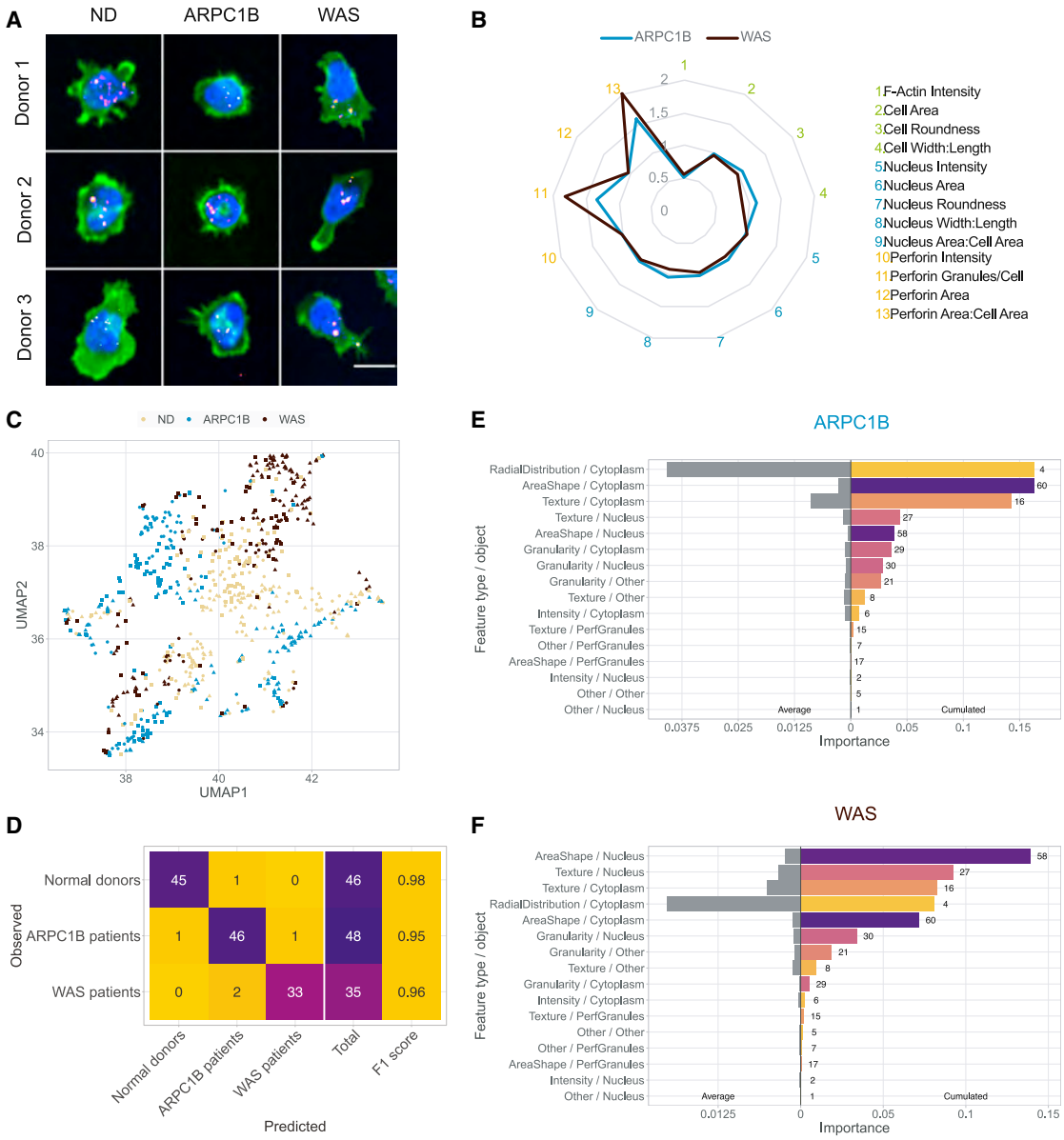

Figure 5. HCI of the IS in WASP- and ARPC1B-deficient CD8$^+$ T cells

(A) Representative images of CD8$^+$ T cells from normal donors and affected individuals, seeded on ICAM-1/anti-CD3 Abs and stained for F-actin (green), perforin granules (yellow), CD8 (red), and nuclei (blue). Scale bars, 10 μm.

(B) Average characteristics of the IS of CD8$^+$ T cells from affected individuals, represented as fold change with respect to the average of three normal donors. The data represent the mean of eight replicates for each sample (24–443 cells per replicate, 2,890–4,881 cells per condition).

(C) UMAP projection of CD8$^+$ T cell morphological profiles. Different shapes denote different samples under each condition (dots, squares, and triangles for the first, second, and third donor/affected individual, respectively).

(D) Confusion matrix and class-wise performance on held-out data of a random forest model trained to discriminate between affected individuals and normal donors.

(E) Total and average importance of morphological features per measurement type and biological object described for prediction of ARPC1B deficiency status.

(F) Total and average importance of morphological features per measurement type and biological object described for prediction of WASP deficiency status.

In (D)–(F), a darker color indicates a higher number of images or descriptors for a given box, and the corresponding count is provided alongside.

positioning in individual normal donor CD8$^+$ T cells at the Z-plane the most proximal to the cell-substrate interface (Figure 6B). The mean minimal distance between lytic granules and the cell edge was considered to account for the radial dispersion of lytic granules. We wanted to find out whether descriptors pertaining to F-actin distribution and cell shape might correlate with lytic granule dispersion. Eight independent variables were found to significantly contribute to the capacity of our model to predict

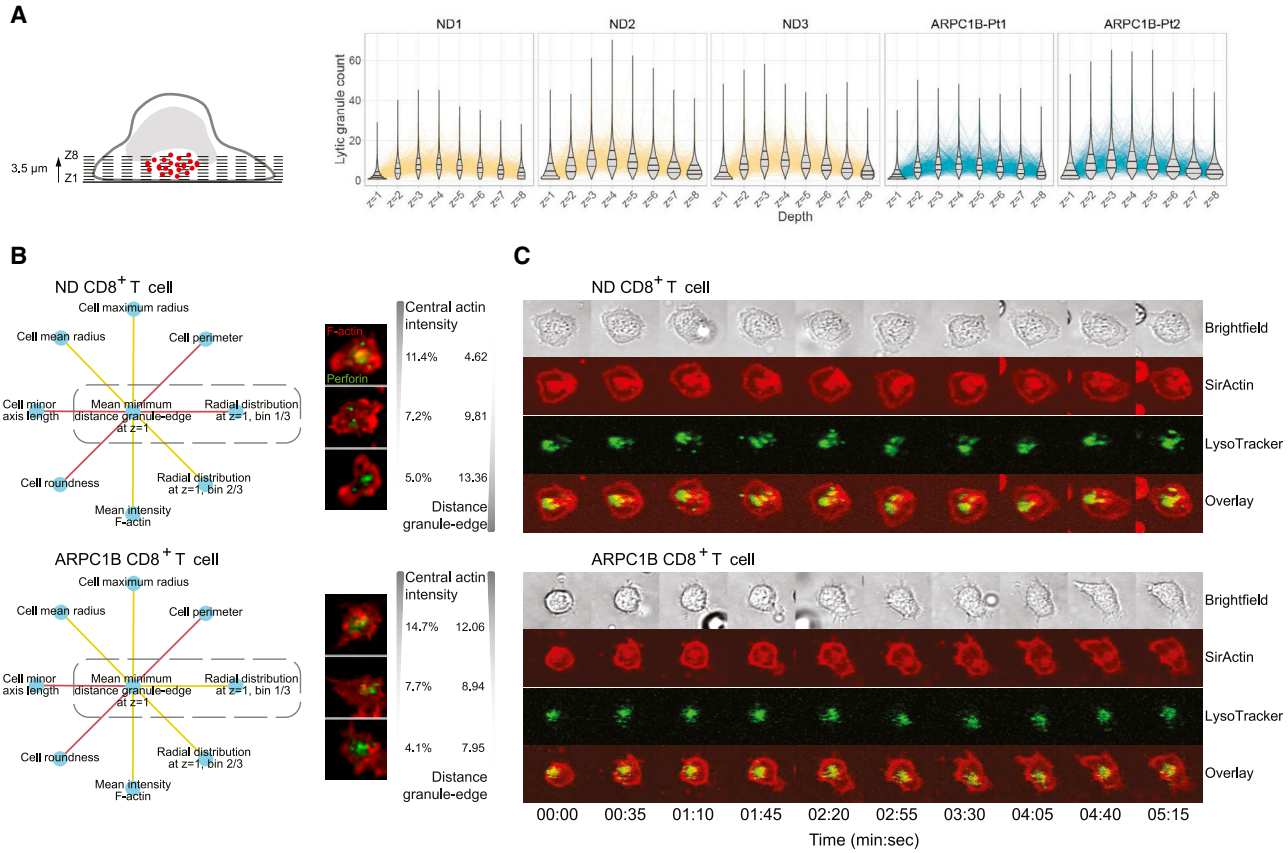

Figure 6. In-depth characterization of ARPC1B deficiency through single-cell analysis of the 3D distribution of lytic granules, granule-actin covariate analysis, and live imaging

(A) Distribution over consecutive focal planes of individual perforin$^+$ objects identified as lytic granules in CD8$^+$ T cells from 3 healthy donors and 2 ARPC1B-deficient individuals upon interaction with ICAM-1 and anti-CD3 Abs.

(B) Positive (green) or negative (red) associations using linear regression of the average minimum distance between the lytic granules and the cell edge based on eight actin-based morphological descriptors at the synapse plane of the indicated cells. Representative images of healthy donor and ARPC1B-deficient CD8$^+$ T cells, showing the relationship between lytic granule and F-actin distribution.

(C) Snapshots of representative video recordings of healthy donor and ARPC1B-deficient CD8$^+$ T cells interacting with an ICAM-1 and anti-CD3 Ab-coated surface and stained with silicon rhodamine (SiR)-actin (red) and LysoTracker (green).

lytic granule dispersion in individual cells (r^2 = 0.2886; Table S3). In particular, our analysis revealed that the radial distribution of F-actin was associated with lytic granule dispersion even when accounting for geometrical confounders. More precisely, the higher the fraction of F-actin intensity at the synapse center, the higher the dispersion of lytic granule toward the cell edges (Figure 6B). This is in line with the notion that partial depletion of F-actin at the IS center is required for lytic granule exocytosis at this site. When this analysis was applied to ARPC1B-deficient T cells, the association of lytic granule dispersion with 7 of the 8 F-actin/shape descriptors held true (Figure 6B; Table S3). However, the association with F-actin density at the IS center was inverted, meaning that higher central F-actin intensity was associated with more central lytic granules (Figure 6B; Table S4). This analysis of parameter correlation at the single-cell level indicates that ARPC1B deficiency disrupts the association between the radial distribution of F-actin and lytic granule positioning. To resolve the temporal aspect of lytic granule dispersion in ARPC1B-deficient CD8$^+$ T cells, we complemented our HCI 3D analysis by time-lapse microscopy using identical stimulatory conditions. We employed a spinning disk microscopy setting to focus on the 1- to 2-µm layer above the IS and acquired images every 35 s. Actin dynamics were visualized with SiR-actin, whereas lytic granules were revealed with LysoTracker. In line with the HCI data, ARPC1B-deficient T cells displayed aberrant IS assembly upon interaction with the stimulatory surface with abnormal cell edge dynamics (Figure 6C; Video S1). In healthy donor and ARPC1B-deficient CD8$^+$ T cells, lytic granules gathered around a ring-like actin structure, presumably corresponding to the previously described peri-centrosomal F-actin network (Obino et al., 2016). However, this F-actin ring and the bulk of lytic granules appeared to oscillate more in ARPC1B-deficient CD8$^+$ T cells and to occupy a less central position compared with their normal counterparts (Figure 6C; Video S1). Our HCI measurements, complemented by live-recording observations, indicate that ARPC1B deficiency does not affect

the overall polarization of the lytic granule pool but affects its dynamic distribution at the synaptic plane. Our analysis points to the aberrant radial organization of the actin cytoskeleton at the IS as a major factor contributing to this defective distribution.

DISCUSSION

By combining automated cell imaging with computational image analysis pipelines, HCI provides novel opportunities to systematically analyze cellular mechanisms (Breinig et al., 2015; Bryce et al., 2019; Rohban et al., 2017). However, the potential of this approach has not yet been explored for the study of immune cells. Here we tailor an HCI approach for high-definition morphological profiling of various human cytotoxic lymphocyte populations and focus on imaging of the IS as a means to capture the responsiveness and effector potential of these cells. We validate our HCI approach by identifying distinct morphological signatures evoked by a panel of actin-targeting drugs. We were thus able to characterize different defects occurring at the IS and how they converge in altering lytic granule positioning. We further reveal the power of our HCI approach to discriminate individual donors on the basis of immune cell morphological traits. We also exemplify the clinical applicability of this approach by identifying cytotoxic lymphocyte aberrations in individuals with severe congenital IEIs.

Conveniently, a simple 2D static approach based on adsorption of stimulatory molecules on the surface microwells was sufficient to robustly stimulate assembly of morphological structures qualifying as ISs. We show that various human lymphocyte populations, including model cell lines, cells freshly isolated from the blood, as well as expanded primary cells, can be stained and imaged with an automated confocal microscope at high resolution in a 384-well format, allowing analysis of several samples, activation conditions, and perturbations in parallel. Computationally, we use robust statistics and work at an image-level resolution, typically gathering a few dozen cells imaged over four Z-planes (along the optical axis) representing the 2-μm section of the cells most proximal to the stimulatory substrate. Although most morphological profiling studies have been limited to average profiles over wells or replicates (Breinig et al., 2015; Caie et al., 2010; Caldera et al., 2019), a few approaches have defined profiles based on single cells (Caicedo et al., 2018; Lu et al., 2019). To compare samples and treatments, we considered the variability in morphology displayed in each image by including measures of dispersion that have been proven to be beneficial for morphological profiles and could potentially be improved by adding a higher-order joint statistical moment (Rohban et al., 2019). We also exploit individual cell heterogeneity to extract relationships among detected descriptors (e.g., F-actin radial distribution and lytic granule dispersion) at single-cell resolution. From an analytical point of view, we elaborate two complementary methods. First, we focus on a pre-defined set of morphological descriptors based on prior knowledge, including cell and nucleus shape parameters as well as intensities of F-actin, LFA-1, and perforin at the synaptic plane. We show that this method can be applied to relatively low numbers of images and provides meaningful identification of discriminative features when comparing experimental conditions. Second, we implement a high-definition and unbiased morphological profiling pipeline from which novel relevant parameters can be identified and high-performance classifiers can be trained to discriminate cell states corresponding to different stimulations, drug treatments, or genetic defects.

Beyond the methodological advance provided in this study, we present data relevant to understanding lymphocyte activation from a fundamental and medically relevant perspective. Among the pre-defined set of morphological descriptors we identify an increase in F-actin as a hallmark of T and NK lymphocyte stimulation by combinations of ICAM-1 and Abs directed against CD3 or NK receptors, respectively. This is in line with the previously established role of the actin cytoskeleton in driving the cell spreading behavior supporting IS assembly (Fritzsche et al., 2017; Roy and Burkhardt, 2018). Further investigation of the role of actin cytoskeleton remodeling by treatment of NK cells with a drug array reveals distinct morphological alterations upon targeting actin polymerization, depolymerization, and myosin II. Our data also point to converging morphologies induced by some of the drugs with distinct modes of action, possibly related to a limited number of configurations of the cytoskeleton, as described recently in an adherent neuroblastoma cell line (Bryce et al., 2019; Yin et al., 2014). Strikingly, most tested drugs yield prominent alteration of the distribution of perforin-containing granules, indicating that the different facets of actin cytoskeleton dynamics are important to regulate polarized delivery of lytic granules at the IS (Carisey et al., 2018; Hetrick et al., 2013). Because of the distinct morphological profiles observed for each drug and detection of dose-dependent effects in cell lines and primary cells, we envision that such an approach could be applied for screening immunotherapeutic drugs.

Application of morphological profiling to lymphocyte populations reveals a previously unappreciated level of heterogeneity in cellular morphological traits among individuals. When considering the data pertaining to NK cells freshly isolated from the blood, we cannot rule out that morphological differences arise from distinct activation states of cells from different donors. However, *in vitro* stimulation and expansion of T lymphocytes, which are expected to robustly drive cells toward a differentiated phenotype (Litterman et al., 2014), were also associated with distinct morphological traits. Further analysis of larger cohorts of donors and sorted subpopulations of lymphocytes, which would be compatible with the approach developed here, will be required to precisely evaluate the degree of morphological heterogeneity among individuals and lymphocyte subsets. The sensitivity of the HCI approach is also highlighted by its ability to distinguish morphological alterations in T lymphocyte populations isolated from individuals suffering from related IEIs. We show that the limited set of IS morphological descriptors (because they might be selected for a classic analysis) suggests an overlap of IS alterations in $CD8^+$ T cells of WASP-deficient and ARPC1B-deficient individuals. However, implementation of high-definition morphological profiling unravels distinct traits for each disease entity, with WASP and ARPC1B deficiencies affecting features of the IS center and periphery, respectively.

Focusing on the recently identified ARPC1B deficiency, we further exemplify the potential of HCI to extract robust quantification of cellular events with high spatial resolution at the single-cell level. In particular, staining of perforin combined with acquisition of 8 confocal planes covering a deep layer of the IS allows

analysis of lytic granule positioning toward the cell-substrate interface. Our 3D analysis indicates that ARPC1B deficiency does not impair lytic granule polarization in the context of 2D synapses. Further analysis of the XY dispersion of lytic granules at the IS plane across normal individual cells reveals numerous correlates with morphological and F-actin-related descriptors, pointing to the covariates that contribute to lytic granule distribution. Interestingly, ARPC1B deficiency appears to reverse the correlation between dispersion of lytic granules and radial distribution of F-actin. These findings motivated complementary investigation of lytic granule and F-actin dynamics by live imaging. Our data indicate that the reduced cytotoxic activity of $CD8^+$ T cells from ARPC1B-deficient individuals is mostly related to loss of coordination between F-actin distribution and lytic granule distribution at the IS plane. Distinct secondary events, such as compensatory mechanisms (e.g., the level of ARPC1A expression) or mutations in other modifier genes, might differentially compensate for the ARPC1B-related defects in the different individuals and explain the more restricted defects we observed in our study (Randzavola et al., 2019; Somech et al., 2017). Our focused study of ARPC1B deficiency illustrates the potential of HCI to provide guidance for implementation of complementary low-throughput assays to assess morphological and functional defects. At this stage, we cannot generalize the case of ARPC1B deficiency in establishing a systematic relationship between IS alteration and functional defects. However, it is interesting that multiple IEIs have been found by us and others to be associated with IS defects and functional impairment (Gil-Krzewska et al., 2018; Kalinichenko et al., 2021; Mace and Orange, 2014; Pfajfer et al., 2017; Salzer et al., 2016). Previous reports have also shown that IEIs where the IS is defective fail to eliminate target cells (Mace and Orange, 2014; Mizesko et al., 2013; Pfajfer et al., 2017). Systematic analysis of multiple such pathologies and corresponding cellular models would certainly provide a unique opportunity to establish rules linking morphology to function.

Here we provide an innovative HCI approach that surpasses current approaches in unbiasedly detecting morphological traits of lymphocyte populations upon activation. We thoroughly report the experimental and computational methods and provide all scripts used in the analysis to maximize the reproducibility of the approach developed here. Further research will be needed to leverage application of HCI to different blood-derived cell subsets, with foreseeable translation into the fields of cancer therapy and personalized medicine.

STAR★METHODS

Detailed methods are provided in the online version of this paper and include the following:

- KEY RESOURCES TABLE
- RESOURCE AVAILABILITY
  - Lead contact
  - Materials availability
  - Data and code availability
- EXPERIMENTAL MODEL AND SUBJECT DETAILS
  - Cell lines and primary cells
  - Patients
- METHODS DETAILS
  - Flow cytometry-based NK-92 cell degranulation
  - Cytotoxicity assay
  - Live microscopy
  - Phenotypic analysis
  - Western blotting
  - Staining for high-content imaging
  - Image acquisition and processing
- QUANTIFICATION AND STATISTICAL ANALYSIS
  - Data processing and visualization
  - Robust morphological perturbation value
  - Random forest models
  - Regression of morphological descriptors

SUPPLEMENTAL INFORMATION

Supplemental information can be found online at https://doi.org/10.1016/j.celrep.2021.109318.

ACKNOWLEDGMENTS

The authors thank Fatima-Ezzahra L'Faqihi-Olive, Valérie Duplan-Eche, Anne-Laure Iscache, and Lydia De La Fuente-Vizuete from the cytometry facility of INFINITy as well as Sophie Allart and Simon Lachambre from the cell imaging facility of INFINITy. We also wish to thank Isabelle Fernandes from the Organoid platform of the IRSD and Muriel Quaranta-Nicaise, Michael Caldera, Raúl Jiménez Heredia, and Marianne Guisset for discussions and technical advice and Alessandro Aiuti, Marco Gattorno, and Stefano Volpi for cell lines derived from affected individuals. This work was supported by the Vienna Science and Technology Fund (WWTF-LS16-060 to K.B., J.M., and L.D. and VRG15-005 to J.M.), the INSERM Plan Cancer program (C15092BS to L.D.), the Association Laurette Fugain (to L.D.), the CNRS IRP program (project SysTact to L.D.), and the Austrian Academy of Science through DOC Fellowship 25365 (to J.H.).

AUTHOR CONTRIBUTIONS

Y.G. performed experiments, analyzed data, and wrote the paper. L.V. designed and performed image data analyses and wrote the paper. A. Kamnev, L.P., J.H., and A. Kalinichenko performed experiments and analyzed data. A.K.M. generated and analyzed cells derived from affected individuals. A.R. contributed to image acquisition. A.F., J.M., and K.B. participated in research design and scientific discussions. L.D. designed the research, supervised the analysis pipeline, and wrote the paper.

DECLARATION OF INTERESTS

The authors declare no competing interests.

Received: May 6, 2020
Revised: February 25, 2021
Accepted: June 7, 2021
Published: July 6, 2021

REFERENCES

Andzelm, M.M., Chen, X., Krzewski, K., Orange, J.S., and Strominger, J.L. (2007). Myosin IIA is required for cytolytic granule exocytosis in human NK cells. J. Exp. Med. *204*, 2285–2291.

Breiman, L. (2001). Random Forests. Mach. Learn. *45*, 5–32.

Breinig, M., Klein, F.A., Huber, W., and Boutros, M. (2015). A chemical-genetic interaction map of small molecules using high-throughput imaging in cancer cells. Mol. Syst. Biol. *11*, 846.

Brigida, I., Zoccolillo, M., Cicalese, M.P., Pfajfer, L., Barzaghi, F., Scala, S., Oleaga-Quintas, C., Álvarez-Álvarez, J.A., Sereni, L., Giannelli, S., et al. (2018). T-cell defects in patients with *ARPC1B* germline mutations account for combined immunodeficiency. Blood *132*, 2362–2374.

Brown, A.C.N., Oddos, S., Dobbie, I.M., Alakoskela, J.-M., Parton, R.M., Eissmann, P., Neil, M.A.A., Dunsby, C., French, P.M.W., Davis, I., and Davis, D.M. (2011). Remodelling of cortical actin where lytic granules dock at natural killer cell immune synapses revealed by super-resolution microscopy. PLoS Biol. *9*, e1001152.

Bryce, N.S., Failes, T.W., Stehn, J.R., Baker, K., Zahler, S., Arzhaeva, Y., Bischof, L., Lyons, C., Dedova, I., Arndt, G.M., et al. (2019). High-Content Imaging of Unbiased Chemical Perturbations Reveals that the Phenotypic Plasticity of the Actin Cytoskeleton Is Constrained. Cell Syst. *9*, 496–507.e5.

Bubb, M.R., Senderowicz, A.M., Sausville, E.A., Duncan, K.L., and Korn, E.D. (1994). Jasplakinolide, a cytotoxic natural product, induces actin polymerization and competitively inhibits the binding of phalloidin to F-actin. J. Biol. Chem. *269*, 14869–14871.

Butler, B., and Cooper, J.A. (2009). Distinct Roles for the Actin Nucleators Arp2/3 and hDia1 during NK-Mediated Cytotoxicity. Curr. Biol. *19*, 1886–1896.

Cabana, E., Lillo, R.E., and Laniado, H. (2019). Multivariate outlier detection based on a robust Mahalanobis distance with shrinkage estimators. Stat. Papers, Published online November 20, 2019. https://doi.org/10.1007/s00362-019-01148-1.

Caicedo, J.C., McQuin, C., Goodman, A., Singh, S., and Carpenter, A.E. (2018). Weakly Supervised Learning of Single-Cell Feature Embeddings. Proc. IEEE Comput. Soc. Conf. Comput. Vis. Pattern Recognit. *2018*, 9309–9318.

Caie, P.D., Walls, R.E., Ingleston-Orme, A., Daya, S., Houslay, T., Eagle, R., Roberts, M.E., and Carragher, N.O. (2010). High-content phenotypic profiling of drug response signatures across distinct cancer cells. Mol. Cancer Ther. *9*, 1913–1926.

Caldera, M., Müller, F., Kaltenbrunner, I., Licciardello, M.P., Lardeau, C.-H., Kubicek, S., and Menche, J. (2019). Mapping the perturbome network of cellular perturbations. Nat. Commun. *10*, 5140.

Carisey, A.F., Mace, E.M., Saeed, M.B., Davis, D.M., and Orange, J.S. (2018). Nanoscale Dynamism of Actin Enables Secretory Function in Cytolytic Cells. Curr. Biol. *28*, 489–502.e9.

Cheminant, M., Mahlaoui, N., Desconclois, C., Canioni, D., Ysebaert, L., Dupré, L., Vasconcelos, Z., Malphettes, M., Moshous, D., Neven, B., et al. (2019). Lymphoproliferative disease in patients with Wiskott-Aldrich syndrome: Analysis of the French Registry of Primary Immunodeficiencies. J. Allergy Clin. Immunol. *143*, 2311–2315.e7.

de Groot, R., Lüthi, J., Lindsay, H., Holtackers, R., and Pelkmans, L. (2018). Large-scale image-based profiling of single-cell phenotypes in arrayed CRISPR-Cas9 gene perturbation screens. Mol. Syst. Biol. *14*, e8064.

De Meester, J., Calvez, R., Valitutti, S., and Dupré, L. (2010). The Wiskott-Aldrich syndrome protein regulates CTL cytotoxicity and is required for efficient killing of B cell lymphoma targets. J. Leukoc. Biol. *88*, 1031–1040.

Dieckmann, N.M.G., Frazer, G.L., Asano, Y., Stinchcombe, J.C., and Griffiths, G.M. (2016). The cytotoxic T lymphocyte immune synapse at a glance. J. Cell Sci. *129*, 2881–2886.

Dupré, L., Aiuti, A., Trifari, S., Martino, S., Saracco, P., Bordignon, C., and Roncarolo, M.-G. (2002). Wiskott-Aldrich syndrome protein regulates lipid raft dynamics during immunological synapse formation. Immunity *17*, 157–166.

Dustin, M.L., and Cooper, J.A. (2000). The immunological synapse and the actin cytoskeleton: molecular hardware for T cell signaling. Nat. Immunol. *1*, 23–29.

Dustin, M.L., and Long, E.O. (2010). Cytotoxic immunological synapses. Immunol. Rev. *235*, 24–34.

Fritzsche, M., Fernandes, R.A., Chang, V.T., Colin-York, H., Clausen, M.P., Felce, J.H., Galiani, S., Erlenkämper, C., Santos, A.M., Heddleston, J.M., et al. (2017). Cytoskeletal actin dynamics shape a ramifying actin network underpinning immunological synapse formation. Sci. Adv. *3*, e1603032.

Gil-Krzewska, A., Saeed, M.B., Oszmiana, A., Fischer, E.R., Lagrue, K., Gahl, W.A., Introne, W.J., Coligan, J.E., Davis, D.M., and Krzewski, K. (2018). An actin cytoskeletal barrier inhibits lytic granule release from natural killer cells in patients with Chediak-Higashi syndrome. J. Allergy Clin. Immunol. *142*, 914–927.e6.

Grakoui, A., Bromley, S.K., Sumen, C., Davis, M.M., Shaw, A.S., Allen, P.M., and Dustin, M.L. (1999). The Immunological Synapse: A Molecular Machine Controlling T Cell Activation. Science 285, 221–227.

Heigwer, F., Scheeder, C., Miersch, T., Schmitt, B., Blass, C., Pour Jamnani, M.V., and Boutros, M. (2018). Time-resolved mapping of genetic interactions to model rewiring of signaling pathways. eLife *7*, e40174.

Hetrick, B., Han, M.S., Helgeson, L.A., and Nolen, B.J. (2013). Small molecules CK-666 and CK-869 inhibit actin-related protein 2/3 complex by blocking an activating conformational change. Chem. Biol. *20*, 701–712.

Houmadi, R., Guipouy, D., Rey-Barroso, J., Vasconcelos, Z., Cornet, J., Manghi, M., Destainville, N., Valitutti, S., Allart, S., and Dupré, L. (2018). The Wiskott-Aldrich Syndrome Protein Contributes to the Assembly of the LFA-1 Nanocluster Belt at the Lytic Synapse. Cell Rep. *22*, 979–991.

Hutz, J.E., Nelson, T., Wu, H., McAllister, G., Moutsatsos, I., Jaeger, S.A., Bandyopadhyay, S., Nigsch, F., Cornett, B., Jenkins, J.L., and Selinger, D.W. (2013). The multidimensional perturbation value: a single metric to measure similarity and activity of treatments in high-throughput multidimensional screens. J. Biomol. Screen. *18*, 367–377.

Joshi, P., and Lee, M.-Y. (2015). High Content Imaging (HCI) on Miniaturized Three-Dimensional (3D) Cell Cultures. Biosensors (Basel) *5*, 768–790.

Kalinichenko, A., Perinetti Casoni, G., Dupré, L., Trotta, L., Huemer, J., Galgano, D., German, Y., Haladik, B., Pazmandi, J., Thian, M., et al. (2021). RhoG deficiency abrogates cytotoxicity of human lymphocytes and causes hemophagocytic lymphohistiocytosis. Blood *137*, 2033–2045.

Krzewski, K., and Coligan, J.E. (2012). Human NK cell lytic granules and regulation of their exocytosis. Front. Immunol. *3*, 335.

Litterman, A.J., Zellmer, D.M., LaRue, R.S., Jameson, S.C., and Largaespada, D.A. (2014). Antigen-specific culture of memory-like CD8 T cells for adoptive immunotherapy. Cancer Immunol. Res. *2*, 839–845.

Lu, A.X., Kraus, O.Z., Cooper, S., and Moses, A.M. (2019). Learning unsupervised feature representations for single cell microscopy images with paired cell inpainting. PLoS Comput. Biol. *15*, e1007348.

Lyubchenko, T.A., Wurth, G.A., and Zweifach, A. (2003). The actin cytoskeleton and cytotoxic T lymphocytes: evidence for multiple roles that could affect granule exocytosis-dependent target cell killing. J. Physiol. *547*, 835–847.

Mace, E.M., and Orange, J.S. (2014). Lytic immune synapse function requires filamentous actin deconstruction by Coronin 1A. Proc. Natl. Acad. Sci. USA *111*, 6708–6713.

Mace, E.M., Wu, W.W., Ho, T., Mann, S.S., Hsu, H.-T., and Orange, J.S. (2012). NK cell lytic granules are highly motile at the immunological synapse and require F-actin for post-degranulation persistence. J. Immunol. *189*, 4870–4880.

Mace, E.M., Dongre, P., Hsu, H.-T., Sinha, P., James, A.M., Mann, S.S., Forbes, L.R., Watkin, L.B., and Orange, J.S. (2014). Cell biological steps and checkpoints in accessing NK cell cytotoxicity. Immunol. Cell Biol. *92*, 245–255.

Mattiazzi Usaj, M., Sahin, N., Friesen, H., Pons, C., Usaj, M., Masinas, M.P.D., Shuteriqi, E., Shkurin, A., Aloy, P., Morris, Q., et al. (2020). Systematic genetics and single-cell imaging reveal widespread morphological pleiotropy and cell-to-cell variability. Mol. Syst. Biol. *16*, e9243.

McInnes, L., Healy, J., Saul, N., and Großberger, L. (2018). UMAP: Uniform Manifold Approximation and Projection. J. Open Source Softw. *3*, 861.

McQuin, C., Goodman, A., Chernyshev, V., Kamentsky, L., Cimini, B.A., Karhohs, K.W., Doan, M., Ding, L., Rafelski, S.M., Thirstrup, D., et al. (2018). CellProfiler 3.0: Next-generation image processing for biology. PLoS Biol. *16*, e2005970.

Mizesko, M.C., Banerjee, P.P., Monaco-Shawver, L., Mace, E.M., Bernal, W.E., Sawalle-Belohradsky, J., Belohradsky, B.H., Heinz, V., Freeman, A.F., Sullivan, K.E., et al. (2013). Defective actin accumulation impairs human

natural killer cell function in patients with dedicator of cytokinesis 8 deficiency. J. Allergy Clin. Immunol. *131*, 840–848.

Monks, C.R.F., Freiberg, B.A., Kupfer, H., Sciaky, N., and Kupfer, A. (1998). Three-dimensional segregation of supramolecular activation clusters in T cells. Nature *395*, 82–86.

Obino, D., Farina, F., Malbec, O., Sáez, P.J., Maurin, M., Gaillard, J., Dingli, F., Loew, D., Gautreau, A., Yuseff, M.-I., et al. (2016). Actin nucleation at the centrosome controls lymphocyte polarity. Nat. Commun. *7*, 10969.

Papakonstantinou, S., and O'Brien, P.J. (2014). High Content Imaging for the Morphometric Diagnosis and Immunophenotypic Prognosis of Canine Lymphomas. Cytometry B Clin. Cytom. Published online February 28, 2014. https://doi.org/10.1002/cytob.21170.

Pfajfer, L., Seidel, M.G., Houmadi, R., Rey-Barroso, J., Hirschmugl, T., Salzer, E., Antón, I.M., Urban, C., Schwinger, W., Boztug, K., and Dupré, L. (2017). WIP deficiency severely affects human lymphocyte architecture during migration and synapse assembly. Blood *130*, 1949–1953.

Priestley, R.S., Cheung, J., Murphy, E.J., Ehebauer, M.T., Davis, J.B., and Di Daniel, E. (2019). A novel high-content imaging-based technique for measuring binding of Dickkopf-1 to low-density lipoprotein receptor-related protein 6. J. Pharmacol. Toxicol. Methods *95*, 47–55.

Randzavola, L.O., Strege, K., Juzans, M., Asano, Y., Stinchcombe, J.C., Gawden-Bone, C.M., Seaman, M.N.J., Kuijpers, T.W., and Griffiths, G.M. (2019). Loss of ARPC1B impairs cytotoxic T lymphocyte maintenance and cytolytic activity. J. Clin. Invest. *129*, 5600–5614.

Rohban, M.H., Singh, S., Wu, X., Berthet, J.B., Bray, M.A., Shrestha, Y., Varelas, X., Boehm, J.S., and Carpenter, A.E. (2017). Systematic morphological profiling of human gene and allele function via Cell Painting. eLife *6*, e24060.

Rohban, M.H., Abbasi, H.S., Singh, S., and Carpenter, A.E. (2019). Capturing single-cell heterogeneity via data fusion improves image-based profiling. Nat. Commun. *10*, 2082.

Rousseeuw, P.J., and Leroy, A.M. (1987). Robust Regression and Outlier Detection (John Wiley & Sons).

Roy, N.H., and Burkhardt, J.K. (2018). The Actin Cytoskeleton: A Mechanical Intermediate for Signal Integration at the Immunological Synapse. Front. Cell Dev. Biol. *6*, 116.

Salzer, E., Cagdas, D., Hons, M., Mace, E.M., Garncarz, W., Petronczki, Ö.Y., Platzer, R., Pfajfer, L., Bilic, I., Ban, S.A., et al. (2016). RASGRP1 deficiency causes immunodeficiency with impaired cytoskeletal dynamics. Nat. Immunol. *17*, 1352–1360.

Sanborn, K.B., Rak, G.D., Maru, S.Y., Demers, K., Difeo, A., Martignetti, J.A., Betts, M.R., Favier, R., Banerjee, P.P., and Orange, J.S. (2009). Myosin IIA associates with NK cell lytic granules to enable their interaction with F-actin and function at the immunological synapse. J. Immunol. *182*, 6969–6984.

Santos, A.M., Ponjavic, A., Fritzsche, M., Fernandes, R.A., de la Serna, J.B., Wilcock, M.J., Schneider, F., Urbančič, I., McColl, J., Anzilotti, C., et al. (2018). Capturing resting T cells: the perils of PLL. Nat. Immunol. *19*, 203–205.

Somech, R., Lev, A., Lee, Y.N., Simon, A.J., Barel, O., Schiby, G., Avivi, C., Barshack, I., Rhodes, M., Yin, J., et al. (2017). Disruption of Thrombocyte and T Lymphocyte Development by a Mutation in *ARPC1B*. J. Immunol. *199*, 4036–4045.

Somersalo, K., Anikeeva, N., Sims, T.N., Thomas, V.K., Strong, R.K., Spies, T., Lebedeva, T., Sykulev, Y., and Dustin, M.L. (2004). Cytotoxic T lymphocytes form an antigen-independent ring junction. J. Clin. Invest. *113*, 49–57.

Vincent, L., and Soille, P. (1991). Watersheds in digital spaces: an efficient algorithm based on immersion simulations. IEEE Trans. Pattern Anal. Mach. Intell. *13*, 583–598.

Wu, L.S., and Li, J. (2018). High-Content Imaging Phenotypic Screen for Neurogenesis Using Primary Neural Progenitor Cells. Methods Mol. Biol. *1787*, 101–113.

Yin, Z., Sailem, H., Sero, J., Ardy, R., Wong, S.T.C., and Bakal, C. (2014). How cells explore shape space: a quantitative statistical perspective of cellular morphogenesis. BioEssays *36*, 1195–1203.

CellPress
OPEN ACCESS

STAR★METHODS

KEY RESOURCES TABLE

REAGENT or RESOURCE	SOURCE	IDENTIFIER
Antibodies		
Mouse anti-human CD3 antibody, clone OKT3	eBiosciences	Cat#16-0037-81; RRID:AB_468854
Mouse anti-human NKp30 antibody, clone P30-15	BioLegend	Cat#325202; RRID:AB_756106
Mouse anti-human NKp30 antibody, clone #210847	R&D systems	Cat#MAB18491; RRID:AB_2149445
Mouse anti-human NKp46 antibody, clone 9-E2	BD PharMingen	Cat#557847; RRID:AB_2149297
Mouse anti-human perforin antibody, clone dG9	Biolegend	Cat#308102; RRID:AB_1085316
Alexa Fluor 647 mouse anti-human perforin antibody, clone dG9	BioLegend	Cat#308110; RRID:AB_493254
PE mouse anti-human granzyme B, clone GB11	BD PharMingen	Cat#561142; RRID:AB_10561690
Pacific Blue mouse anti-human CD8 antibody, clone SK1	BioLegend	Cat#344718; RRID:AB_10551438
PE mouse anti-LAMP1 antibody, clone eBioH4A3	eBioscience	Cat#12-1079-42; RRID:AB_10853326
Alexa Fluor 700 mouse anti-human CD56 antibody, clone B159	BD biosciences	Cat#557919; RRID:AB_396940
Mouse anti-human anti-LFA-1 (CD11a) antibody, clone HI-111	BioLegend	Cat#301202; RRID:AB_314140
Alexa Fluor 647 goat anti-mouse IgG1 cross-adsorbed secondary antibody	ThermoFisher Scientific	Cat#A-21240; RRID:AB_2535809
Alexa Fluor 555 goat anti-mouse IgG2b cross-adsorbed secondary antibody	ThermoFisher Scientific	Cat#A-21147; RRID:AB_141778
Mouse anti-GAPDH antibody, clone 6C5	Santa Cruz Biotechnology	Cat#32233; RRID:AB_627679
Mouse anti-HSP90 antibody, clone F-8	Santa Cruz Biotechnology	Cat#13119; RRID:AB_675659
Anti-WASP rabbit polyclonal antibody	Santa Cruz Biotechnology	Cat#sc-8353; RRID:AB_794067
Anti-ARPC1B rabbit polyclonal antibody	Sigma Aldrich	Cat#HPA004832; RRID:AB_1845044
HRP-conjugated anti-rabbit IgG antibody	Cell Signaling	Cat#7074S; RRID:AB_2099233
Biological samples		
Peripheral blood from healthy donors	Etablissement Français du Sang (EFS Occitanie)	N/A
Peripheral blood mononuclear cells from 3 ARPC1B- and 3 WASP-deficient patients (all male subjects)	San Raffaele Hospital, Milan Italy ; Saint Anna Children's Hopital, Vienna, Austria; Institut Universitaire du Cancer de Toulouse - Oncopole, Toulouse, France	Somech et al., 2017 Brigida et al., 2018 Dupré et al., 2002 De Meester et al., 2010 Cheminant et al., 2019
Chemicals, peptides, and recombinant proteins		
Phalloidin-Alexa Fluor 488	ThermoFisher Scientific	Cat#A12379
4′,6-diamidino-2-phenylindole, DAPI	ThermoFisher Scientific	Cat#D1306; RRID:AB_2629482
Recombinant human ICAM-1/Fc chimera	R&D systems	Cat#720-IC
Ionomycin	Sigma-Aldrich	Cat#I0634-5MG
Phorbol 12-myristate 13-acetate, PMA	Sigma-Aldrich	Cat#79346-1MG
Latrunculin B	Abcam	Cat#ab144291
Jasplakinolide	Calbiochem	Cat#420127-50UG
Blebbistatin	Sigma-Aldrich	Cat#B0560-1MG
Y-27632	Calbiochem	Cat#68802-1MG
Arp2/3 Complex Inhibitor II, CK-869	MedChemExpress	Cat#HY-16927-10mM/1ml
Wiskostatin	Sigma-Aldrich	Cat#W2270-5MG
Formin FH2 Domain Inhibitor, SMIFH2	Calbiochem	Cat#344092-10MG

(*Continued on next page*)

Continued

REAGENT or RESOURCE	SOURCE	IDENTIFIER
Dimethyl sulfoxide, DMSO	Sigma-Aldrich	Cat#41640-1L-M
Phytohaemagglutinin, PHA	ThermoFisher Scientific	Cat#R30852801
Recombinant human IL-2	Peprotech	Cat#200-02
Aphidicolin	Sigma Aldrich	Cat#A0781
CellTrace Violet	ThermoFisher Scientific	Cat#C34571
Fibronectin	Sigma Aldrich	Cat#F1141-1MG
Cell Tracker green CMFDA	ThermoFisher Scientific	Cat#C7025
SiR-actin	Tebu-bio	Cat#SC001
LysoTracker Blue	ThermoFisher Scientific	Cat#L7525
Protease and Phosphatase Inhibitor Cocktail	ThermoFisher Scientific	Cat#78442
Poly-L-Lysine Solution (0.01%)	Merck	Cat#A-005-C
Paraformaldehyde 16%, EM grade	ThermoFisher Scientific	Cat#50-980-489
Critical commercial assays		
EasySep Human $CD8^+$ T cell enrichment kit	StemCell	Cat#19053
MagniSort Human NK enrichment kit	Invitrogen	Cat#8804-6819
Super Signal West Pico Chemiluminescence Substrate	ThermoFisher Scientific	Cat#34080
Deposited data		
Morphological measurements	This manuscript	FigShare: https://doi.org/10.6084/m9.figshare.11619960
Experimental models: Cell lines		
NK-92 lymphoblastic natural killer cell line, originating from the peripheral blood of a male subject	ATCC	Cat#CRL-2407; RRID:CVCL_2142
Jurkat lymphoblastic T cell line, originating from the peripheral blood of a male subject	ATCC	Cat#TIB-152; RRID:CVCL_0367
P815 mastocytoma cell line of murine origin (DBA/2 strain)	ATCC	Cat#TIB-64; RRID:CVCL_2154
Software and algorithms		
FlowJo	BD	FlowJo 10.7.2
R	The R Foundation	R 3.5.1
Excel	Microsoft	1902
umap-learn	McInnes et al., 2018	0.3.6
robustbase	CRAN	0.93
randomforest	CRAN	4.6
CellProfiler	McQuin et al., 2018	3.0
ggplot2	CRAN	3.1.1
Harmony high-content imaging and analysis software	PerkinElmer	HH17000012
Analysis notebooks	This manuscript	Zenodo: https://doi.org/10.5281/zenodo.4562363
Other		
CellCarrier-384 Ultra Microplates	PerkinElmer	Cat#6057300

RESOURCE AVAILABILITY

Lead contact

Further information and requests for resources and reagents should be directed to and will be fulfilled by the lead contact, Loïc Dupré (loic.dupre@inserm.fr).

Materials availability

Raw images of individual experimental sets can be obtained upon request.

Data and code availability

All the CellProfiler pipelines and morphological measurements used in this analysis are made available on FigShare with the DOI 10.6084/m9.figshare.11619960. The analyses can be found and reproduced using the Docker image and scripts provided via Zenodo: https://doi.org/10.5281/zenodo.4562363

EXPERIMENTAL MODEL AND SUBJECT DETAILS

Cell lines and primary cells

Jurkat cells were cultured in RPMI (GIBCO) supplemented with 10% FBS, 100 U/ml penicillin/streptomycin, 1 mM sodium pyruvate, 1X non-essential amino acids and 10 mM HEPES (all from ThermoFisher Scientific). NK-92 cells were cultured according to the recommendations from ATCC. Primary NK cells were purified from freshly isolated PBMCs using the MagniSort Human NK enrichment kit (Invitrogen) and maintained in RPMI supplemented with 5% human serum, 100 U/ml penicillin/streptomycin, 1 mM sodium pyruvate, 1X non-essential amino acids and 10 mM HEPES. Primary $CD8^+$ T cells were purified from frozen PBMCs of three healthy donors, three ARPC1B-deficient patients and three WASP-deficient patients by negative selection using the EasySep Human $CD8^+$ T cell enrichment kit (StemCell Technologies, Inc.). $CD8^+$ T cells were stimulated in RPMI supplemented with 5% human serum, 100 U/ml penicillin/streptomycin, 1 mM sodium pyruvate, 1X non-essential amino acids, 10 mM HEPES, 1 μg/ml PHA and 100 IU/ml IL-2. $CD8^+$ T cells were expanded for further rounds every two weeks with a mixture of irradiated PBMCs from three normal donors. Peripheral blood from healthy donors and patients was obtained in accordance with the 1964 Helsinki declaration and its later amendments or ethical standards. Informed consents were approved by the relevant local Institutional Ethical Committees.

Patients

ARPC1B Patient 1 (ARPC1B-Pt1, male, 15 years) corresponds to Pt1 in the study by Brigida et al. (2018). The patient carries a c.64+1G > C splice donor variant in the *ARPC1B* gene resulting in insertion of 21 nucleotides from intron 2 and usage of an alternative splice site with partial intron retention and maintenance of the reading frame. ARPC1B-Pt1 was initially described as having a subpopulation (21%) of T cells expressing normal levels of ARPC1B (as detected by flow cytometry), possibly resulting from a secondary mutation. However, expanded $CD8^+$ T cells failed to express ARPC1B (Figure S5B). ARPC1B-Pt2 (male, 2 months) corresponds to Pt2 in the study by Somech et al. (2017) and to Pt7 in the study by Brigida et al. (2018). ARPC1B-Pt2 carries a 2-bp deletion (n.c.G623DEL-TC) causing a putative frameshift resulting in premature termination (p.V208VfsX20). The ARPC1B protein was not detected (short fragment could theoretically be expressed but remain undetected; see Figure S5B). ARPC1B Pt3 (male, 4 years) is a patient with early disease onset. He carries an homozygous 2-bp duplication (c.613_614dup), leading to a frameshift and premature termination (p.H206YfsX16). ARPC1B protein failed to be detected by western blotting in the T cells from the patient (Figure S5B). WAS-Pt1 (male, 1 year) corresponds to patient WAS1 in the study by De Meester et al. (2010). WAS-Pt1 carries a *WAS* gene nonstop mutation (c.1509A > C), resulting in undetectable WASP expression in the PBMC-derived $CD8^+$ T cells (Figure S5A). WAS-Pt2 (male, 5 years) corresponds to patient WAS2 in the study by Dupré et al. (2002). WAS-Pt2 carries a 2-nucleotide deletion (ag) in exon 4 (position 484 to 485) resulting in a stop codon (codon 167). Accordingly, no WASP expression was detected in the expanded $CD8^+$ T cells from the patient (Figure S5A). WAS-Pt3 (male, 51 years) corresponds to patient P10 in the study by Cheminant et al. (2019). WAS-Pt3 carries a c.1453G > A mis-splicing mutation. This patient was reported to express revertant WASP in a minor fraction of peripheral lymphocytes. However we failed to detect WASP expression in the expanded $CD8^+$ T cells from the patient (Figure S5A).

METHODS DETAILS

Flow cytometry-based NK-92 cell degranulation

NK-92 cells were incubated for 1 hr with Blebbistatin (5, 10 and 50 μM), CK-869 (10, 25 and 50 μM), Jasplakinolide (0.1, 1 and 2.5 μM), Latrunculin B (0.1, 0.25 and 0.5 μM), SMIFH2 (50, 100 and 250 μM), Wiskostatin (10, 50 and 100 μM), Y-27632 (5, 10 and 25 μM) and DMSO as control (all drugs from Merck). For stimulation cells were transferred into a 96 well plate (Nunc MaxiSorp) coated overnight at 4°C with 5 μg/ml anti-NKp30 Ab and 0.4 μg/ml recombinant human ICAM-1-Fc chimera (R&D Systems) in PBS, briefly spun down and further incubated in the presence of chemical compounds and anti-CD107a Ab for 4 hr. Following incubation, NK-92 cells were stained with anti-CD56 and anti-CD107a Ab for 30 min, washed, fixed and analyzed using LSR-Fortessa flow cytometer.

Cytotoxicity assay

Target P815 cells were stained for 30 min with Cell Tracker green CMFDA (ThermoFisher Scientific) and coated with 0 to 10 μg/ml anti-CD3 Ab (OKT3, eBiosciences) for one hour at 37°C. They were also treated with 0.2 μg/ml aphidicolin to prevent proliferation during assessment of killing. $CD8^+$ T cells were stained in parallel with CellTrace Violet (CTV, ThermoFisher Scientific). Stained P815 and $CD8^+$ T cells were seeded at a 1 to 1 ratio in a 384-well plate precoated with 1 μg/ml fibronectin and incubated at 37°C, 5% $C0_2$ for 24 hr. Cells were imaged on an automated spinning disk confocal HCS device (Opera Phenix, PerkinElmer) with a 20x objective, necessitating 25 fields of view per well for full surface coverage. Residual alive target cells were counted automatically with the Harmony software on the basis of their size and CMFDA staining. Percentage of killing was calculated as 100 - (100 x residual alive target cells / unexposed target cells).

Live microscopy

Eight-well chamber slides (IbiTreat, ibidi) were coated overnight with 4 μg/ml recombinant human ICAM-1-Fc chimera (R&D Systems) and 10 μg/ml anti-CD3 Ab (OKT3, eBiosciences) at 4°C. Cells were stained with 2 μM SiR-actin (tebu-bio) and 1 μM LysoTracker Blue (ThermoFisher Scientific) for 1 hr at 37°C before transfer to the pre-warmed coated slides. Cells were imaged on a Nikon inverted spinning disk confocal microscope equipped with an oil immersion 40X objective (NA 1.3), a SCMOS camera (6.5 μm/pixels) and a temperature and CO_2 controlled chamber. Acquisition of SiR-actin, LysoTracker Blue and DIC were done over multiple wells at 1 image every 35 s for a total of 61 frames.

Phenotypic analysis

Expanded $CD8^+$ T cells from normal donors and ARPC1B-deficient patients were stained with fluorochrome-coupled Ab recognizing the extracellular markers CD8 (BioLegend) and LFA-1 (BioLegend) for 30 min at 4°C. Intracellular staining was performed following fixation and permeabilization, with Ab specific for perforin (BioLegend) and granzyme B (BD Pharmigen) for 45 min at 4°C. The data were acquired on a MacsQuant Q10 (Miltenyi) and analyzed with FlowJo. Student's t test was used to calculate significance.

Western blotting

Cell extracts were prepared from 10×10^6 expanded $CD8^+$ T cells. Briefly, T cells were washed in PBS and resuspended in RIPA lysis buffer (Millipore), supplemented with protease and phosphatase inhibitor cocktail (ThermoFisher Scientific). After 20 min on ice, lysates were cleared by centrifugation. Laemmli sample buffer (BioRad) was added to supernatants and, after boiling, samples were subjected to SDS-PAGE. Proteins were transferred to nitrocellulose membranes (GE Healthcare). WASP and ARPC1B were detected with, respectively, anti-WASP Ab (H-250, Santa Cruz Biotechnology) and anti-ARPC1B Ab (HPA004832, Sigma Aldrich), followed by secondary HRP-conjugated anti-rabbit Ab (Cell Signaling). Control of protein loading was performed by hybridizing the same membranes with anti-GAPDH or anti-HSP90 Abs (both from Santa Cruz Biotechnology). Detection was performed using the Super Signal West Pico Chemiluminescence Substrate (ThermoFisher Scientific).

Staining for high-content imaging

CellCarrier-384 Ultra tissue culture treated plates (PerkinElmer) were coated with either 0.1 mg/ml poly-L-lysine (Merck) or a combination of 2 μg/ml recombinant human ICAM-1-Fc chimera (R&D Systems), 1 μg/ml NKp30 (MAB18491, R&D systems) and 1 μg/ml NKp46 (557487, BD Biosciences). NK-92 cells were cultured in IL-2 free medium overnight. NK-92 cells or primary NK cells were seeded at 15000 and 5000 cells per well, respectively and incubated for 30 min at 37°C. Cells were fixed with 3% paraformaldehyde (ThermoFisher Scientific) and stained with anti-perforin Ab (dG9, Biolegend) and phalloidin-AF 488 (ThermoFisher Scientific). AF 555-conjugated goat anti-mouse IgG2b Ab (ThermoFisher Scientific) was used to reveal perforin staining. Nuclei were stained with DAPI (ThermoFisher Scientific).

NK-92 cells were treated with 5, 10 and 50 μM Blebbistatin, 10, 25 and 50 μM CK-869, 0.1, 1 and 2.5 μM Jasplakinolide, 0.1, 0.25 and 0.5 μM Latrunculin B, 50, 100 and 250 μM SMIFH2, 10 50 and 100 μM Wiskostatin and 5, 10 and 25 μM Y-27632 (all drugs from Merck) for 30 min at 37°C and washed twice in PBS before seeding onto the plates and letting them adhere for 30 min. The same procedure was applied to primary NK cells treated with 5, 10, 25 and 50 μM CK-869 and 25 50, 100 and 250 μM SMIFH2.

CellCarrier-384 Ultra tissue culture treated plates were coated with either 0.1 mg/ml poly-L-lysine or a combination of 2 μg/ml recombinant human ICAM-1-Fc chimera (R&D Systems) and 10 μg/ml anti-CD3 Ab (OKT3, eBioscience). Jurkat cells or untransformed $CD8^+$ T cells were seeded at 10000 and 5000 cells per well, respectively and incubated for 15 min at 37°C. Cells were fixed with 3% paraformaldehyde and stained with anti-LFA-1 Ab (clone HI-111, BioLegend) and phalloidin-AF 488 (ThermoFisher Scientific) in permeabilization buffer (eBioscience). AF 647-conjugated goat anti-mouse IgG1 Ab (ThermoFisher Scientific) was used to reveal LFA-1 staining. $CD8^+$ T cells were in addition stained with anti-perforin Ab and AF 555-conjugated goat anti-mouse Ab (ThermoFisher Scientific) was used to reveal perforin staining. Where indicated, cells were stained with anti-CD8 Ab instead of anti-LFA-1 Ab. Nuclei were stained with DAPI. Stained cells were kept in PBS at 4°C until imaging. Comparisons of samples or treatments were done within the same staining/acquisition batches, as well as within the same plates to avoid possible bias due to staining intensity variability. To account for possible well-to-well variability, each well was replicated at least 3 times.

Image acquisition and processing

Images were acquired on an automated spinning disk confocal HCS device (Opera Phenix, PerkinElmer) equipped with a 40x 1.1 NA Plan Apochromat water immersion objective and 4 sCMOS cameras (16 bits, 2160 × 2160 pixels, 6.5 μm pixel size), allowing simultaneous acquisition in 4 channels. For each well, 40 automatically selected fields and 8 Z-planes per field (0.5 μm step, starting from the cell-substrate contact plane) were acquired, making use of a spinning microlens disk. For the experiment on primary NK cells, only 31 fields of view and 6 Z-planes were imaged, while 13 fields and 13 Z-planes were imaged in the experiment on WASP- and ARPC1B-deficient patients. Where indicated, stacks of images were combined with maximum projection of 4 focal slices in proximity of the cell-substrate contact plane (*z* from 2 to 5 with a 0.5 μm step). Image datasets were processed with CellProfiler 3.0 (McQuin et al., 2018) (see Data and code availability). In brief, the image quality was assessed, the intensities for experiments with high background noise were log-transformed, the illumination on each image was corrected based on background intensities, and DNA precipitations were avoided by multiplying intensities on DAPI channel by phalloidin intensities before segmenting cell

nuclei using global minimum cross entropy thresholding. A secondary segmentation of the cytoplasms was performed using the watershed method (Vincent and Soille, 1991) and global minimum cross entropy thresholding on the phalloidin channel. Image sets with low maximal DNA intensity or showing no nucleus were discarded. Cells having more than 30% of their cytoplasm surface at less than 5 pixels of another cell were removed, in order to ignore clusters of cells and to focus on single cells displaying an IS. Small actin speckles in the cytoplasm at more than 3 pixels from the membrane as well as speckles of perforin and secondary objects spanned around the nuclei by LFA-1 staining were segmented. Additionally, primary NK and expanded $CD8^+$ T cells with low CD8 intensities (if stained) or associated with less than two perforin granules were excluded from the analysis. Finally, measurements were acquired for colocalization of these objects, intensities in the nuclei and cytoplasms, granularity on all channels, textural and shape features, intensity distributions, distance and overlap between objects, number of speckles and neighbors less than 10 pixels away. The average and the standard deviation per field of view of these features were kept. This led to 1898 and 2076 morphological features in NK-92 and Jurkat cells respectively. For primary NK cells and expanded patient $CD8^+$ T cells, features related to actin speckles were excluded, as they were not found to be informative, resulting in 2386 and 1780 features, respectively.

QUANTIFICATION AND STATISTICAL ANALYSIS

Data processing and visualization

Analyses in R 3.5.1 with the data visualization package ggplot2 3.1.1 and Microsoft Excel (Version 1902) were subsequently conducted. A smaller set of informative morphological features was selected and the quality of processed images was checked by (i) removing wells with low maximal DNA intensity and cell count, (ii) removing features and images generating missing values and (iii) removing constant features in the study dataset or the subset of negative controls used as reference. From these images passing our quality checks, up to 16 raw summary variables were extracted, based on their interpretability and on their known relevance to describe the IS. The fold changes compared to unstimulated or untreated controls were further reported and displayed in the form or radar charts. On the other hand, for all features, per-image values X were transformed successively with the following functions f_1 and f_2, with $X_{Control}$ the negative controls in X on which the dataset is normalized:

$$f_1(X) = log(X + 1 - (X))$$

$$f_2(X) = \frac{X - median(X_{Control})}{mad(X_{Control})}$$

To remove redundancy in the set of features used for downstream analyses, we ensured that the selected variables were not excessively linearly correlated. To do so, all features were ordered from highest to lowest median absolute deviation (hence by variation in the experiment compared to negative controls). Starting from the top of this list, all other features linearly correlated to the first feature with a Pearson's coefficient higher than 0.6 were excluded. We sequentially went on with the next remaining feature in the list and iterated until the acquisition of a small and informative set of uncorrelated features. This led to 383 of such features for the drug screen on NK-92 (Figure 3) and 306 for the experiment on ARPC1B- and WASP-deficient patients (Figure 5), coined comprehensive morphological descriptors. This set of features was used for visualization and quantification of the overall morphological changes induced by perturbations. The dimensionality of the data was reduced using the UMAP algorithm (McInnes et al., 2018) to two dimensions for visualizations and three dimensions for computation of the statistical significance of morphological effects in the drug screen on NK-92. This pipeline succeeded in selecting a wide range of features that were not excessively biased by confounders (Figure S3B).

Robust morphological perturbation value

To quantify the significance of overall changes in morphology between a perturbed state and a reference state (healthy or untreated cells), we defined the Robust Morphological Perturbation Value (RMPV). This extends the concept of Multidimensional Perturbation Value (Hutz et al., 2013) which defines a single value summarizing the statistical significance of morphological changes in multidimensional spaces, by using robust statistics and the minimum covariance determinant (Rousseeuw and Leroy, 1987) decreasing the sensitivity to technical (unfiltered artifacts) and biological outliers (images displaying extreme morphologies or uncommon cell states). In brief, the RMPV is obtained for X the set of all filtered and uncorrelated features and X_{WT} the subset of the data corresponding to images of the reference population in five steps. First, the minimum covariance determinant estimator $M(X_{WT})$ is calculated to describe the variation of morphologies observed in the reference set, using its implementation in the R package *robustBase* version 0.93. Second, this value is used to determine R, the robust Mahalanobis distance of each images of X to X_{WT} (Cabana et al., 2019). Third, the median value $\tilde{R} = medain(R)$ was obtained for each drug tested. Fourth, for 2000 iterations the labels of the condition and the reference were randomly permuted to obtain an empirical distribution of $\tilde{R}$ under the assumption that there was no difference between the multivariate location and scatter of the morphological parameters of the perturbation and the reference. Finally, the RMPV is defined as the empirical p value obtained from these distributions after FDR adjustment for testing changes in multiple conditions and indicates the probability of observing at least half of the images displaying morphological changes of a similar intensity if the perturbation was similar to the reference.

Random forest models

We used the random forest algorithm (Breiman, 2001) with its implementation in the R package *randomForest* version 4.6 and built classifier models to characterize the strength and types of the morphological changes observed and identify what was specific of each cellular condition (chemical perturbation or disease state). In brief, the algorithm generates a set of decision trees. Each tree is constructed to minimize the number of misclassified entries of a bootstrap sample of the training data by choosing between a fixed number *mtry* of randomly selected input features at each split. The final prediction of the model is the most common one out of the predictions of all individual trees. We trained the model on the comprehensive set of informative and uncorrelated morphological features measured per image – previously used for dimensionality reduction. Each forest included 1000 decision trees. The dataset was split in 6 folds of equal size (459 feature vectors per fold for the treated NK cells and 126 for the ARPC1B- and WASP-deficient patient cells), each containing all possible classification labels. To select the optimal number *mtry* of variables selected at each split, we incremented the parameter value from 20 to 90 by steps of 10 and assessed the performance using the macro F_1 score as defined below in a 5-fold cross-validation scheme. One extra fold was used as validation set to estimate the performance of the model after selection of the optimal parameters and retraining on all of the 5 folds used for cross-validation. In the case of the drug screen on the NK-92 cell line, we used a similar approach using the 13 features of known relevance in describing the IS as input, and testing *mtry* values from 1 to 13 with steps of 3. Overall, the performance was evaluated using the macro F_1 score:

$$F_1 = \frac{1}{n}\sum_{i=1}^{n}\frac{2 \times TP_i}{2 \times TP_i + FP_i + FN_i}$$

where n is the number of categories in the classification, and TP_i, FP_i and FN_i are respectively the number of true positives, false positives and false negatives for category i in the validation set. To interpret the feature importance in the prediction, the mean decrease in accuracy obtained when including each feature was extracted, either for the prediction of a given class or overall using micro averaging. The total and average importance of features split in distinct groups based on the type of measurements and biological object described were calculated as well. These feature groups were defined based on the corresponding CellProfiler measurement types and biological objects. Features that did not describe the cytoplasm, nucleus, perforin granules or actin granules were counted in the "Other" biological object category. Similarly, features that did not correspond to the "Texture," "AreaShape," "RadialDistribution," "Granularity" or "Intensity" measurements were grouped under the term "Other."

Regression of morphological descriptors

For the single-cell morphological measurements of ARPC1B-deficient patients and normal donors (Figures 6A and 6B), we modeled the average radial position of lytic granules per cell, defined as the minimum number of pixels between a perforin granule and the edge of the segmented cell, in terms of eight other measurements based on the actin staining, using a multiple least-square regression with intercept. These covariates were describing the geometry of the cell ("AreaShape_Perimeter," "AreaShape_FormFactor," "AreaShape_MeanRadius," "AreaShape_MaximumRadius," "AreaShape_MinorAxisLength"), the total average actin intensity ("Intensity_MeanIntensity_CorrActin") as well as the radial distribution of the actin at the synaptic plane ("RadialDistribution_FracAtD_CorrActin1_1of3" and "RadialDistribution_FracAtD_CorrActin1_2of3"). To note, this corresponds to the intensity fraction when separating the cell in three concentric regions centered on the nucleus and numbered from 1, for the space directly surrounding the nucleus, to 3, for the edge of the cell. The third bin was not included in the model as it is purely redundant to the information contained in bins 1 and 2. Three separate models were obtained across cells from all three normal donors, ARPC1B-Pt1 and ARPC1B-Pt2, respectively (Table S3).

Cell Reports, Volume *36*

Supplemental information

Morphological profiling of human T and NK lymphocytes by high-content cell imaging

Yolla German, Loan Vulliard, Anton Kamnev, Laurène Pfajfer, Jakob Huemer, Anna-Katharina Mautner, Aude Rubio, Artem Kalinichenko, Kaan Boztug, Audrey Ferrand, Jörg Menche, and Loïc Dupré

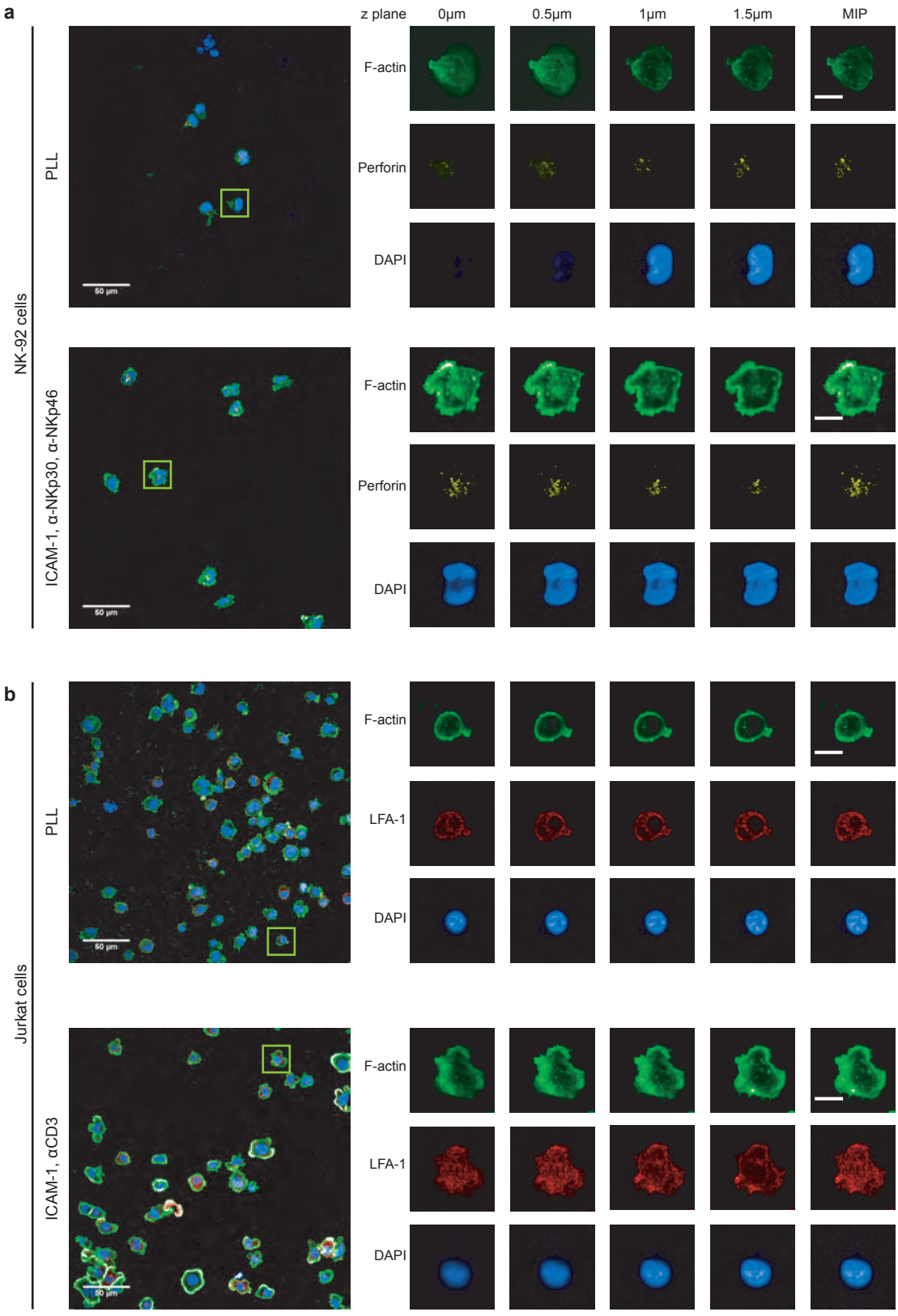

Figure S1 | Individual channels and z planes of single cells isolated from representative fields of view. a. Maximum intensity projection (MIP) of a representative field of view of NK-92 cells seeded on PLL (top) or ICAM-1, anti-NKp30 and NKp-46 (bottom), with zoom on a single representative cell stained for F-actin (green), perforin granules (yellow) and nuclei (DAPI) imaged at 4 z-planes with a step of 0.5 µm and its MIP. **b**. MIP of a representative field of view of Jurkat cells seeded on PLL (top) ICAM-1, anti-CD3 (bottom), with zoom on a single cell stained for F-actin (green), LFA-1 (red) and nuclei (DAPI) and imaged at 4 z-planes with a step of 0.5 µm and its MIP. Scale bars: Field of view 50 µm and single cell 10 µm. Related to Figure 1.

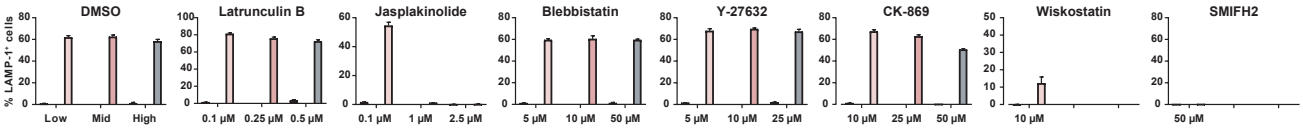

Figure S2 | Actin-targeting drugs differentially affect lytic granule exocytosis in NK-92 cells. Percentage of LAMP-1$^+$ NK-92 cells upon stimulation with coated ICAM-1 and anti-NKp30 Ab. DMSO or actin-targeting drugs were tested at the indicated concentrations. Histograms correspond to mean ± SD of triplicate measurements. Related to Figure 2.

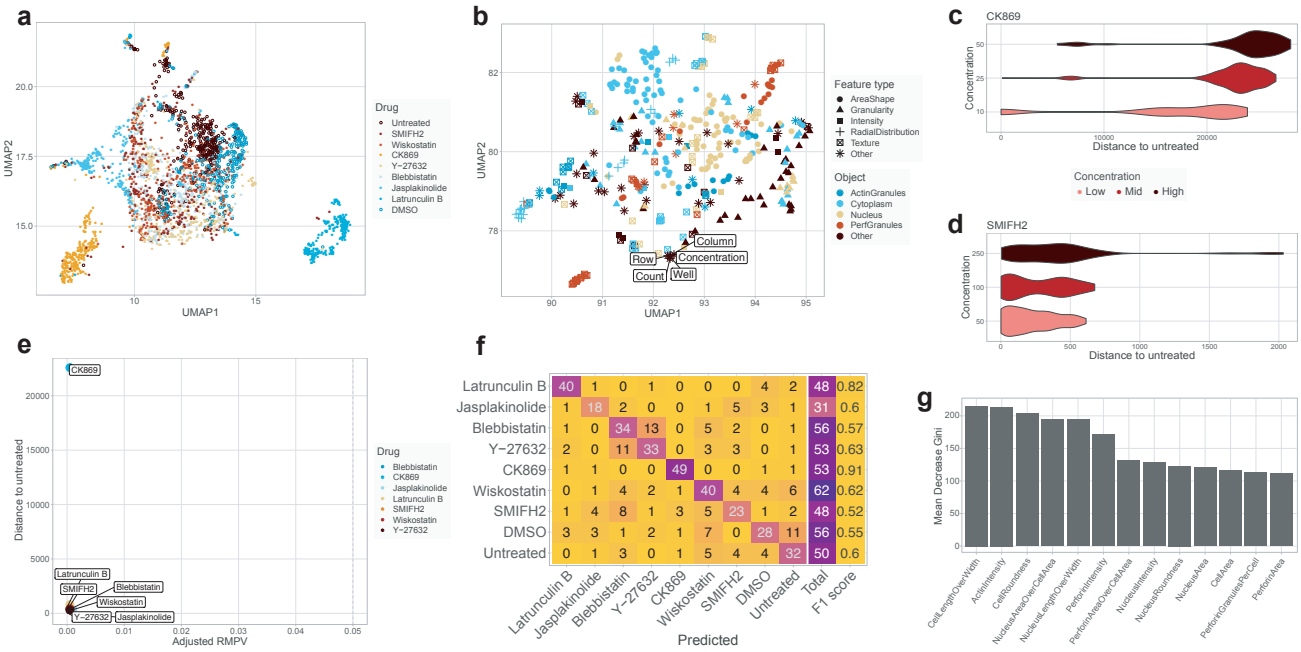

Figure S3 | Drug treatment leads to distinct immunological synapse phenotypes in NK-92 cells. a. Confusion matrix and class-wise performance of a random forest model trained to predict drug treatment based on 13 curated morphological descriptors of NK-92 seeded on ICAM-1, anti-NKp30 and anti-NKp46. **b**. Importance of the 13 morphological descriptors for the classification described in panel (**a**). **c**. UMAP representing the clustering of all the drugs and the untreated conditions. **d**. UMAP representing the relations between confounders and morphological descriptors, obtained by fitting the UMAP on the transpose of the data underlying panel (**c**). **e-f**. Violin plots representing the effect size of drug concentrations on morphological descriptors for (**e**) CK-869 and (**f**) SMIFH2. **g**. FDR-corrected Robust Morphological Perturbation Value (RMPV) of the different drugs. Related to Figure 3.

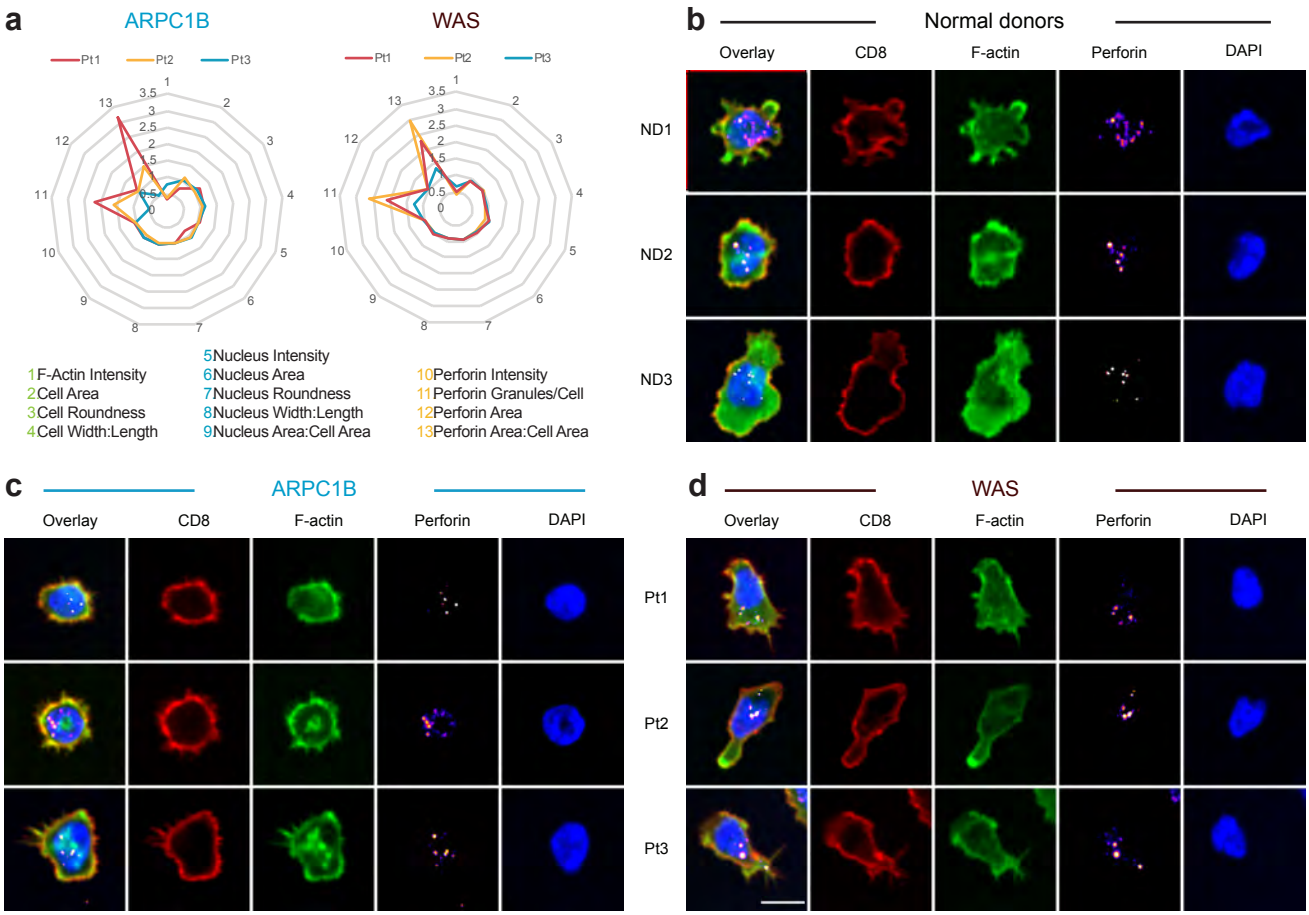

Figure S4 | Individual morphology of patient CD8⁺ T cells. a. Average characteristics of the IS of CD8+ T cells from patients represented as fold change with respect to the average of three normal donors (312-3091 cells per donor or patient). **b-d.** Representative images of CD8+ T cells from (**b**) normal donors, (**c**) ARPC1B-deficient or (**d**) WASP-deficient patients. Scale bar: 10 µm. Related to Figure 5.

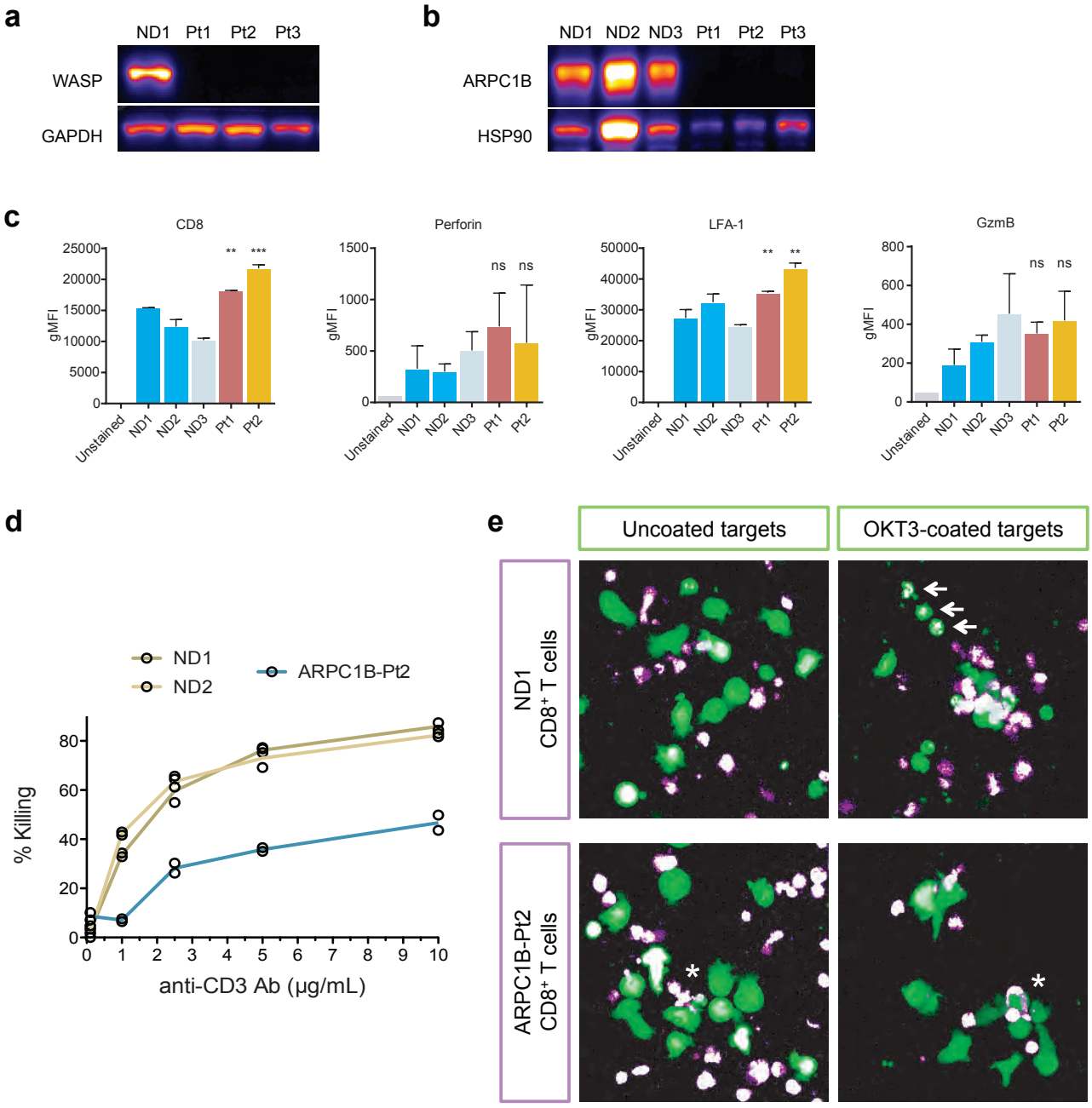

Figure S5 | Phenotypic and functional charaterization of CD8⁺ T cells a-b. Western blot analysis of WASP AND ARPC1B expression in the corresponding patients. **c**. Expression levels of CD8, perforin, LFA-1 and granzyme B in the indicated T cells. **d**. Cytotoxic activity of CD8⁺ T cells against anti-CD3-coated P815 target cells. **e**. Representative images of the interaction of CD8⁺ T cells (purple) with P815 target cells (green). Arrows point to dead target cells. Stars point to ARPC1B-deficient T cells with aberrant morphologies. Related to figure 5 and 6.

	NK-92		
	PLL	ICAM-1, α-NKp30, α-NKp46	Fold increase
F-Actin intensity	0.065098277	0.110223848	1.69319149
Cell Area (μm^2)	2469.321237	3130.618434	1.26780525
Cell Roundness	0.674079624	0.444435641	0.65932217
Cell Width:Length	0.686074044	0.71563093	1.04308119
Nucleus Intensity	0.067203031	0.067329026	1.00187485
Nucleus Area(μm2)	1037.718811	1333.179255	1.2847211
Nucleus Roundness	0.706061099	0.689874902	0.97707536
Nucleus Width:Length	0.685545171	0.706542199	1.03062822
Nucleus Area:Cell Area	0.427455169	0.431859895	1.01030453
Perforin Intensity	0.018403047	0.018502314	1.00539403
Perforin Granules/Cell	13.04941437	16.7196273	1.28125499
Perforin Area(μm2)	86.05831253	117.5449158	1.36587521
Perforin Area:Cell Area	0.035039484	0.036882184	1.05258922

Table S1 | Mean values and fold increase of immunological synapse parameters in NK-92 cells. Mean values of individual parameters pertaining to the immunological synapse in NK-92 cells seeded on PLL or ICAM-1, anti-NKp30 and anti-NKp46, and the fold change of the ratio of each mean value on the stimulated condition with respect to PLL. Intensity is measured in arbitrary units and area in μm^2. Related to Figure 1.

	Jurkat		
	PLL	ICAM-1, α-CD3	Fold increase
F-Actin intensity	0.000289437	0.000437181	1.5104544
Cell Area(μm2)	1921.009837	2690.327023	1.4004754
Cell Roundness	0.530654443	0.61184158	1.15299436
Cell Width:Length	0.800192404	0.767932394	0.95968468
Nucleus Intensity	0.07313481	0.074429279	1.01769975
Nucleus Area(μm2)	879.0221429	995.945146	1.13301486
Nucleus Roundness	0.830340643	0.806271514	0.97101295
Nucleus Width:Length	0.779080494	0.754652368	0.96864493
Nucleus Area:Cell Area	0.460560432	0.379756314	0.82455263
LFA-1 Intensity	0.006679646	0.007880989	1.17985131
LFA-1 Area(μm2)	1728.306565	2526.153065	1.46163483
LFA-1 Area:Cell Area	0.900646361	0.938478533	1.04200558

Table S2 | Mean values and fold increase of immunological synapse parameters in Jurkat cells. Mean values of individual parameters pertaining to the immunological synapse in Jurkat cells seeded on PLL or ICAM-1 and anti-CD3, and the fold change of the ratio of each mean value on the stimulated condition with respect to PLL. Intensity is measured in arbitrary units and area in μm^2. Related to Figure 1.

Normal donors	Estimate	Std. Error	t value	Pr(>|t|)
Intercept	-0.205921	0.1595205	-1.291	0.196754
AreaShape_Perimeter	-0.004858	0.0005022	-9.674	< 2e-16
AreaShape_MaximumRadius	0.4582657	0.0158259	28.957	< 2e-16
AreaShape_MinorAxisLength	-0.0095155	0.0030981	-3.071	0.002132
AreaShape_MeanRadius	0.3306122	0.0440017	7.514	5.86E-14
AreaShape_FormFactor	-0.7657327	0.2011575	-3.807	0.000141
Intensity_MeanIntensity_CorrActin	7.0413384	0.585683	12.022	< 2e-16
RadialDistribution_FracAtD_CorrActin1_1of3	-3.0109743	0.4111895	-7.323	2.47E-13
RadialDistribution_FracAtD_CorrActin1_2of3	3.8917133	0.2652633	14.671	< 2e-16
Adjusted R-squared: 0.2884				

ARPC1B-Pt1	Estimate	Std. Error	t value	Pr(>|t|)
Intercept	0.8029111	0.2525619	3.179	0.00148
AreaShape_Perimeter	-0.0049727	0.0009152	-5.433	5.61E-08
AreaShape_MaximumRadius	0.5992636	0.0273474	21.913	< 2e-16
AreaShape_MinorAxisLength	-0.0060863	0.0072368	-0.841	0.400351
AreaShape_MeanRadius	0.0203988	0.0722717	0.282	0.777754
AreaShape_FormFactor	-0.751234	0.2694728	-2.788	0.005313
Intensity_MeanIntensity_CorrActin	5.0379313	1.3418843	3.754	0.000174
RadialDistribution_FracAtD_CorrActin1_1of3	-0.7157633	0.4704314	-1.522	0.128152
RadialDistribution_FracAtD_CorrActin1_2of3	1.3439737	0.3781638	3.554	0.000381
Adjusted R-squared: 0.2878				

ARPC1B-Pt2	Estimate	Std. Error	t value	Pr(>|t|)
Intercept	0.0541722	0.180384	0.3	0.763939
AreaShape_Perimeter	-0.004052	0.0004741	-8.546	< 2e-16
AreaShape_MaximumRadius	0.5642439	0.0207764	27.158	< 2e-16
AreaShape_MinorAxisLength	-0.0157821	0.0043454	-3.632	0.000282
AreaShape_MeanRadius	0.11303	0.0553829	2.041	0.041274
AreaShape_FormFactor	-1.1368577	0.2379435	-4.778	1.78E-06
Intensity_MeanIntensity_CorrActin	6.7594643	1.1084589	6.098	1.09E-09
RadialDistribution_FracAtD_CorrActin1_1of3	2.5718437	0.5322001	4.832	1.36E-06
RadialDistribution_FracAtD_CorrActin1_2of3	1.4839242	0.352878	4.205	2.62E-05
Adjusted R-squared: 0.324				

Table S3 | Coefficient values in linear models of the distance between lytic granules and cell edges based on morphological descriptors in single lymphocytes. Related to Figure 6.

Donor	Row	Column	Field	X	Y	Mean minimum distance granule-edge at z=1	Cell perimeter	Cell maximum radius	Cell minor axis length	Cell mean radius	Cell roundness	Mean intensity F-actin	Radial distribution at z=1, bin 1/3	Radial distribution at z=1, bin 2/3
ND3	14	8	9	387.75	230.75	4.61511	193.924	18.1108	39.2498	6.61522	0.56706	0.068513	0.11376	0.300318
ND1	3	8	17	734.60385	602.26538	9.81357	198.888	19.0263	42.6223	6.79265	0.567696	0.0646902	0.0723923	0.277189
ND2	4	15	32	172	406.5	13.3571	212.409	17.4642	42.2882	6.60718	0.546465	0.0654103	0.0497074	0.271457
ARPC1B-Pt2	10	13	22	334.70238	591.58333	12.0592	228.859	18.6011	41.7853	6.29407	0.394436	0.0539251	0.146708	0.29765
ARPC1B-Pt2	9	14	27	394.80949	975.90586	8.93749	254.38	18.6815	41.0687	6.2795	0.377715	0.0587798	0.0765422	0.280822
ARPC1B-Pt2	9	14	18	671.72049	157.47093	7.95421	232.001	19	40.6662	6.31474	0.391061	0.0525494	0.0407361	0.276465

Table S4 | Morphological descriptors values of representative cells. The cells are described in the same order as shown in Figure 6b. In the CellProfiler analysis, the corresponding parameters in the table are respectively called 'Mean_FilterNKPerfGranules1_Location_Center_X', 'Mean_FilterNKPerfGranules1_Location_Center_Y', 'Mean_FilterNKPerfGranules1_Distance_Minimum_FilterNKCytoplasm', 'AreaShape_Perimeter', 'AreaShape_MaximumRadius', 'AreaShape_MinorAxisLength', 'AreaShape_MeanRadius', 'AreaShape_FormFactor', 'Intensity_MeanIntensity_CorrActin', 'RadialDistribution_FracAtD_CorrActin1_1of3' and 'RadialDistribution_FracAtD_CorrActin1_2of3'. Related to Figure 6.